Check for updates

ORIGINAL PAPER

M. A. Langthjem

On the mechanism of flutter of a flag

Abstract This paper is concerned with the dynamics and stability of a flapping flag, with emphasis on the onset of flutter instability. The mathematical model is based on the one derived in a paper by Argentina and Mahadevan (Proc Nat Acad Sci 102:1829–1834, 2005). In that paper, it is reported that the effect of vortex shedding from the trailing edge of the flag, represented by the complex Theodorsen function C, has a stabilizing effect, in the sense that the critical flow speed (where flutter is initiated) is increased significantly when vortex shedding is included. The numerical eigenvalue analyses of the present paper display the opposite effect: the critical flow speed is decreased when the Theodorsen function (i.e., vortex shedding) is included. These predictions are verified by an analytical energy balance analysis, where it is proved that a small imaginary part of the Theodorsen function, $C = 1 - \mathrm{i}\,\epsilon, 0 < \epsilon \ll 1$, has a destabilizing effect, i.e., the critical flow speed is smaller than by the so-called quasi-steady approximation $C = 1 - \mathrm{i}\,0$. Furthermore, order-of-magnitude considerations show that Coriolis and centrifugal force terms in the equation of motion, previously discarded on the assumption that they are associated with very slow changes across the flag, have to be retained. Numerical results show that these terms have a significant effect on the stability of the flag; specifically, the said destabilizing effect of the vortex shedding is significantly reduced when these terms are retained. The mentioned energy balance analysis illuminates the nature of the flutter oscillations and the 'competition', at the flutter threshold, between the different types of fluid forces acting on the flag.

1 Introduction

The mechanical and mathematical understanding of flapping flags and sails has been of interest to many scientists through more than a century. It seems that the first theoretical investigation of a flapping flag is due to Rayleigh [29]. In an investigation of the instability of jets, published in 1879, Rayleigh noted that 'its bearing upon the flapping of sails and flags will be evident.' Rayleigh's investigation is included in Lamb's *Hydrodynamics* [16, p. 374], and its relation to the flapping of flags and sails is mentioned therein, too.

Until the start of the twenty-first century, the general scientific interest in the flag problem was not large but still, a number of noteworthy studies were published. Thwaites [39] studied theoretically the fluid–structure interaction problem of flow past a flexible, inelastic membrane. Taneda [35] carried out a careful experimental study of the waving motion of flags in a wind tunnel. Coene [9] investigated, both theoretically and experimentally, the stability of a long 'flag' (a fabric strip) subjected to tension. Coene writes that the investigation actually gives the solutions to two examples (problems) formulated in Milne-Thomson's *Theoretical Hydrodynamics* [25, p. 466], of which the second one reads, 'Explain, giving the necessary theory, why a flag flaps

M. A. Langthjem (✉)
Faculty of Engineering, Yamagata University, 4-3-16 Jonan, Yonezawa, Yamagata 992-8510, Japan
E-mail: mikael@yz.yamagata-u.ac.jp

M. A. Langthjem

in a breeze.' Fitt and Pope [13] formulated a mathematical model which included the mass and stiffness of the flag.

At the dawn of the twenty-first century, new experimental studies seem to have revitalized the interest in the classical flag problem. Zhang et al. [42] studied the dynamics of flexible filaments in a flowing soap film as a model for a one-dimensional flag in a two-dimensional flow. Shelley et al. [31] carried out experiments on a flexible sheet, as a model of a heavy flag, in flowing water. Many new theoretical investigations, as well as new experiments, have appeared in the wake of the extended understanding obtained through these papers. Some of them (up to 2011) are described in a review paper by Shelley and Zhang [32].

The present investigation was motivated by the work of Argentina and Mahadevan [2] and, in particular, by their discussion of the mechanism of instability in terms of asymptotic limits. Specifically, they discuss the limit where the nondimensional mean flow speed $u \to \infty$ while the added fluid mass parameter

$$\rho = \frac{\text{fluid density}}{\text{flag density}} \frac{\text{flag length}}{\text{flag thickness}} \to 0$$

in such a way that the dynamic fluid pressure (and fluid force multiplier) term ρu^2 is finite. In this limit, the complex Theodorsen function becomes real, $C \to 1 - \mathrm{i}\,0$. This function, which represents the vortex shedding from the trailing edge of the flag, acts as a multiplier to the fluid force terms, and $C = 1 - \mathrm{i}\,0$, called the quasi-steady approximation, corresponds to the neglect of vortex shedding. Numerical results in [2] show that in this limit, the critical flow speed is significantly lower when this quasi-steady approximation ($C = 1 - \mathrm{i}\,0$) is used in place of the true, complex value of C. They show also that, in this limit, the flutter oscillations are dominated by the first (fundamental, free vibration) eigenmode, while in the quasi-steady approximation, coupled-mode flutter, with a coupling between the first and the second eigenmode, takes place. These results appear to differ from classical results for flutter of cantilevered plates in an airstream (e.g. [27, Ch. 6.8]).

How can a very small imaginary part of C have such a large influence on the critical flow speed? And how can the quasi-steady critical flow speed—characterized by coupled-mode flutter—be so much lower than the properly evaluated 'unsteady' critical flow speed which, apparently, is characterized by single-mode flutter in first eigenmode? It was the main motivation behind the present study to clarify such questions through analytical energy considerations, supported by computations.

The paper is organized as follows. Section 2 reviews and develops the fluid force evaluation and the coupled fluid–structure equation of motion derived by Argentina and Mahadevan [2]. It is argued that some terms neglected in [2]—specifically, fluid force terms of Coriolis and centrifugal force type—need to be retained in the equation of motion. Discretization of this equation of motion, as well as the determination of eigenvalues and eigenvectors, is discussed in Sect. 3.

Section 4 is concerned with a numerical stability analysis, i.e., the determination of eigenvalues as functions of the flow speed u, and flutter oscillations. Special attention is paid to the influence of the Theodorsen function, in order to understand that, in [2], the critical flow speed is increased significantly when vortex shedding is taken into account, as discussed above. In the present numerical analysis, the opposite effect is found, that is, that the critical flow speed is decreased significantly when the effect of vortex shedding is taken into account. A possible reason for this is discussed, and it is emphasized that the sign of the argument of the Theodorsen function must be considered carefully.

On the other hand, it is found that the 'destabilizing effect' of the vortex shedding (and thus, of the Theodorsen function) is largely reduced when the mentioned Coriolis and centrifugal force terms are properly taken into account. It is also found that the inclusion of these terms implies that higher-order eigenmodes are brought into play in the flutter oscillations, as seen by experiments with flag-like thin structures [27,40].

Section 5 is concerned with energy considerations. The main result of that section is a proof that the presence of a small imaginary part in the Theodorsen function C will actually lower the critical flow speed, relative to the value for quasi-steady limit, $C = 1 - \mathrm{i}\,0$, in full support of the numerical results of Sect. 4. The energy balance analysis contributes also to an extended understanding of the nature of the flutter oscillations. It is shown, for example, that a necessary condition for flutter to occur is that the gradient of the phase angle function is negative over most part of the flag domain. Finally, conclusions are made in Sect. 6.

2 Equation of motion

The undisturbed flag lies in the domain $0 \le x \le L$, $y = 0$, $0 \le z \le l$, where (x, y, z) is a usual right-hand Cartesian coordinate system, with the z-axis orthogonal to the x- and y- axes and running into the paper, see
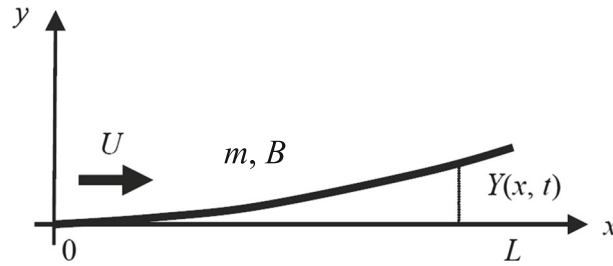
Fig. 1 Sketch of the flapping flag configuration. The width of the flag is l (into the paper)

Fig. 1. A fluid of density ρ_f is moving with uniform velocity U in the positive x-direction. The flag is modeled as a thin plate, and it is assumed that this plate vibrates only in beam modes; that is, at any point $x \in [0, L]$, the deflection is the same for any $z \in [0, l]$.

Let $Y(x, t)$ be the deflection of the flag at position x and time t. Then, the equation of motion is given by

$$m \frac{\partial^2 Y}{\partial t^2} + B^* \frac{\partial^5 Y}{\partial^4 x \partial t} + B \frac{\partial^4 Y}{\partial x^4} = l \Delta P. \tag{1}$$

Here, $m = \rho_s h l$ is the mass per unit length of the flag, where ρ_s is the density of the flag material of thickness h, $B = E h^3 / 12(1 - v^2)$ is the flexural rigidity, where E is Young's modulus and v is Poisson's ratio, B^* is a parameter that represents internal damping in the flag material and ΔP is the pressure difference across the flag due to the fluid flow.

Assuming that the flag/plate is clamped at $x = 0$ and free at $x = L$, the four boundary conditions are given by

$$Y(0, t) = 0, \quad \left[\frac{\partial Y}{\partial x} \right]_{x=0} = 0,$$
$$\left[\frac{\partial^2 Y}{\partial x^2} \right]_{x=L} = 0, \quad \left[\frac{\partial^3 Y}{\partial x^3} \right]_{x=L} = 0. \tag{2}$$

Argentina and Mahadevan [2] have carried out an analysis of the fluid forces acting on the flag, based on the classical work of Theodorsen [38]. In their analysis, they evaluate a non-circulatory velocity potential ϕ_{nc} to account for the flow along the flag and a circulatory velocity potential ϕ_{c} to account for the vortex wake shed from the trailing edge of the flag, in order to satisfy the Kutta–Joukowski condition as well as Kelvin's theorem [3,22]. Making use of the linearized Bernoulli equation

$$p(x, y, t) = -\rho_f \left[\frac{\partial}{\partial t} + U \frac{\partial}{\partial x} \right] \phi(x, y, t), \tag{3}$$

where p is the pressure and $\phi = \phi_{\text{nc}} + \phi_{\text{c}}$, the pressure difference across the flag is evaluated as

$$\Delta P = -\rho_f U C(\kappa) f \left(\frac{x}{L} \right) \left\{ \frac{\partial Y}{\partial t} + U \frac{\partial Y}{\partial x} \right\}$$
$$- \rho_f L g \left(\frac{x}{L} \right) \left\{ \frac{\partial^2 Y}{\partial t^2} + 2U \frac{\partial^2 Y}{\partial t \partial x} + U^2 \frac{\partial^2 Y}{\partial x^2} \right\}. \tag{4}$$

Here,

$$f(\xi) = 2\sqrt{\frac{1 - \xi}{\xi}}, \quad g(\xi) = 2\sqrt{(1 - \xi)\xi}, \tag{5}$$

and $C(\kappa)$ is the Theodorsen function, to be specified a little later. The functions $f(\xi)$ and $g(\xi)$ are shown in Fig. 2. It is noted that they are both positive definite for $0 \leq \xi \leq 1$.

It is noted also that Argentina and Mahadevan [2] discard the last two terms in (4) on the ground that they are small in comparison with the first term of the second line. It will be shown a little later that this is not the case.
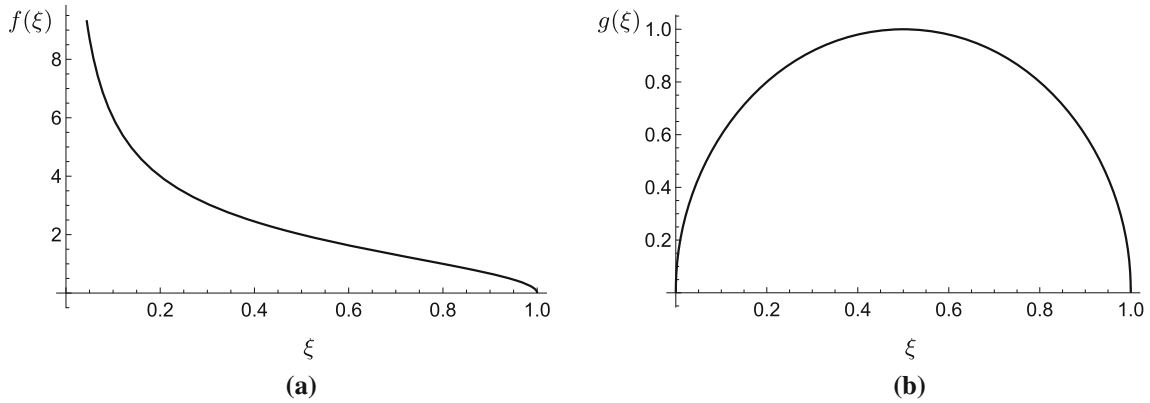
Fig. 2 Functions $f(\xi)$ (**a**) and $g(\xi)$ (**b**) defined in (5)

In the following, we will make use of nondimensional versions of (1) and (2) which can be obtained by introducing the nondimensional parameters

$$\xi = \frac{x}{L}, \quad \tau = \frac{t}{L}U_B = \frac{t}{L}\frac{1}{L}\sqrt{\frac{B}{m}}, \quad \eta = \frac{Y}{L},$$

$$\rho = \frac{\rho_f L l}{m} = \frac{\rho_f}{\rho_s}\frac{L}{h}, \quad u = \frac{U}{U_B} = UL\sqrt{\frac{m}{B}}, \quad \sigma^* = \frac{B^*}{B}U_B, \tag{6}$$

where U_B is the elastic wave propagation speed. Equations (1) and (2) then take the forms

$$\{1 + \rho g(\xi)\}\frac{\partial^2 \eta}{\partial \tau^2} + \sigma^*\frac{\partial^5 \eta}{\partial \xi^4 \partial \tau} + \frac{\partial^4 \eta}{\partial \xi^4} + \rho u C(\kappa) f(\xi)\left\{\frac{\partial \eta}{\partial \tau} + u\frac{\partial \eta}{\partial \xi}\right\}$$

$$+ \rho u g(\xi)\left\{2\frac{\partial^2 \eta}{\partial \xi \partial \tau} + u\frac{\partial^2 \eta}{\partial \xi^2}\right\} = 0, \tag{7}$$

and

$$\eta(0, \tau) = 0, \quad \left[\frac{\partial \eta}{\partial \xi}\right]_{\xi=0} = 0,$$

$$\left[\frac{\partial^2 \eta}{\partial \xi^2}\right]_{\xi=1} = 0, \quad \left[\frac{\partial^3 \eta}{\partial \xi^3}\right]_{\xi=1} = 0. \tag{8}$$

The first term in (7) represents inertia forces, with the term multiplying unity (in the first pair of curly brackets) being the inertia forces of the flag itself and the term multiplying $\rho g(\xi)$ the inertia forces due to the added fluid mass. The second term represents dissipative forces due to internal damping of the flag material. The third term represents the elastic forces of the flag. The fourth term, proportional to ρu, represents dissipative forces due to fluid damping. The fifth and final term in the first line, proportional to ρu^2, represents circulatory fluid forces. The two terms in the second line are fluid force terms as well, originating from the last two terms in (4). The first term (in the second line) represents Coriolis forces, while the second term represents a 'centrifugal force' [26].

It is noted that $\partial^2 Y/\partial t^2 = (U_B^2/L)\partial^2 \eta/\partial \tau^2$, $2U\partial^2 Y/\partial t\partial x = (U_B^2/L)2u\partial^2 \eta/\partial \tau \partial \xi$, and $U^2\partial^2 Y/\partial x^2 = (U_B^2/L)u^2\partial^2 \eta/\partial \xi^2$, that is to say, the three terms in the last line of (4) are of the same order of magnitude; the last two terms cannot be neglected. It follows from (7) that the fluid force terms in the second line are of same order of magnitude as the last two terms in the first line; again, they *cannot* be neglected.

The Theodorsen function $C(\kappa)$ is defined by

$$C(\kappa) = \frac{\displaystyle\int_1^\infty \frac{\tilde{\xi}}{\sqrt{\tilde{\xi}^2 - 1}}e^{-i\kappa\tilde{\xi}}d\tilde{\xi}}{\displaystyle\int_1^\infty \sqrt{\frac{\tilde{\xi} + 1}{\tilde{\xi} - 1}}e^{-i\kappa\tilde{\xi}}d\tilde{\xi}} = \frac{H_1^{(2)}(\kappa)}{H_1^{(2)}(\kappa) + iH_0^{(2)}(\kappa)}, \quad \kappa \in \mathbb{R}_+, \tag{9}$$

where $H_n^{(2)}$ is the Hankel function of second kind and order n, and

$$\kappa = \frac{\omega}{2u} \tag{10}$$

is a nondimensional, real, positive wavenumber, with ω being the nondimensional frequency of the flag oscillations (defined in connection with (11)). The function C represents the vortex wake shed from the trailing edge $\xi = 1$, modeled by the mentioned non-circulatory potential ϕ_{nc}, and as indicated by (9), it involves evaluation of integrals over the shed vorticity in the domain $\tilde{\tilde{\xi}} \in [1, \infty)$; see [2,5,14,38] for details. (In particular, Theodorsen himself [38] gives a step-by-step evaluation of the improper integrals into Bessel and Hankel functions.) Thus, κ, defined by (10), is the wavenumber for the oscillating vortex sheet representing the wake from the flag and will in the following be called the wake wavenumber.

In the numerical stability analyses to follow, the time dependence of the solution $\eta(\xi, \tau)$ is assumed to be in the form

$$\eta(\xi, \tau) = \hat{\eta}(\xi) \exp(\lambda \tau), \tag{11}$$

with $\lambda = \alpha + \mathrm{i}\omega$. Inserting (11) into (7) turns the latter equation into an ordinary differential equation which, together with the boundary conditions (8), constitutes an eigenvalue problem. With reference to (11), the vibrations are stable if $\alpha < 0$ and unstable if $\alpha > 0$. The stability limit SL and the critical flow speed u_c are defined as follows: SL $= \{(u, \alpha) : \alpha = 0 \text{ for } u = u_c, \alpha > 0 \text{ for } u > u_c\}$. Flutter is initiated at SL $(u = u_c)$ if $\omega \neq 0$, divergence if $\omega = 0$. In case of flutter (which is the only type of instability considered in the present paper), the imaginary part ω of the leading (latently unstable) eigenvalue branch (or eigenvalue curve) $\lambda = \lambda(u)$ at the critical flow speed u_c is called the flutter frequency and is denoted by ω_c, where the subscript c indicates 'critical'.

Considering the time dependence given by (11), it may be more natural to replace $\mathrm{i}\kappa = \mathrm{i}\omega/2u$ in the first expression in (9) by $\lambda/2u = (\alpha + \mathrm{i}\omega)/2u$. But, as noted by Bisplinghoff et al. [5, p. 281], this implies that the integrals become divergent by stable motion, i.e. for $\alpha < 0$. Such a representation is thus not feasible. On the other hand, it is possible and of interest to extend (9) to include negative values of ω. (It is possible because both positive and negative values of ω correspond to an outgoing wake; cf. [2,5,14,38].) We find that [1]

$$C(-\kappa) = \frac{H_1^{(1)}(\kappa)}{H_1^{(1)}(\kappa) - \mathrm{i}H_0^{(1)}(\kappa)}, \quad \kappa \in \mathbb{R}_+, \tag{12}$$

where $H_n^{(1)}$ is the Hankel function of first kind, order n. It is seen that (12) is simply the complex conjugate of (9).

3 Discretization and eigensolution analysis

The boundary value problem obtained from (7), (8), and (11) is solved numerically by employing a Galerkin finite element discretization. The flag is divided into N_e elements, each of length $1/N_e$. Within each element, the deflection η is approximated by cubic polynomials [10, p. 101]. Equations (7) and (8) are then transformed into a matrix eigenvalue problem in the form

$$\mathbf{L}(\lambda)\mathbf{a} = \left[\lambda^2 \left\{\mathbf{M}_s + \rho \mathbf{M}_f\right\} + \lambda \mathbf{D}_s + \mathbf{S} + \rho u C(\kappa) \left\{\lambda \mathbf{D}_f + u\mathbf{F}\right\} + \rho u \left\{2\mathbf{C} + u\mathbf{G}\right\}\right]\mathbf{a} = \mathbf{0}, \tag{13}$$

where $\mathbf{M}_s$ is the structural mass matrix, $\mathbf{M}_f$ is the added (fluid) mass matrix, $\mathbf{D}_s$ is the structural damping matrix, $\mathbf{S}$ is the stiffness matrix, $\mathbf{D}_f$ is the fluid damping matrix (proportional to the term $\partial \eta/\partial \tau$ in (7)), $\mathbf{F}$ is a fluid load matrix, $\mathbf{C}$ is a Coriolis matrix, $\mathbf{G}$ is a second fluid load matrix and $\mathbf{a} = \mathbf{a}_R + \mathrm{i}\mathbf{a}_I$ is the complex eigenvector, with $\mathbf{a}_R$ being the real part and $\mathbf{a}_I$ the imaginary part. The matrices $\mathbf{M}_s, \mathbf{M}_f, \mathbf{D}_s, \mathbf{D}_f$, and $\mathbf{S}$ are symmetric, $\mathbf{F}$ and $\mathbf{C}$ are skew-symmetric, while $\mathbf{G}$ is generally non-symmetric. With the column divided into N_e elements, the matrices in (13) are of size $2N_e \times 2N_e$, as each node has two degrees of freedom (deflection and rotation).

Since $\kappa = \text{Im}(\lambda)/2u$, (13) is a nonlinear eigenvalue problem. The eigenvalues λ are determined by employing a Newton–Raphson method [17, p. 81]. Let λ_s be approximation number s to an eigenvalue. Then, the improved approximation, number $s + 1$, is given by

$$\lambda_{s+1} = \lambda_s - \frac{\mathbf{b}_s^T \mathbf{L}(\lambda_s)\mathbf{a}_s}{\mathbf{b}_s^T \mathbf{L}_{,\lambda}(\lambda_s)\mathbf{a}_s}, \quad s = 0, 1, \ldots \tag{14}$$

where $\mathbf{b}$ is the left eigenvector, given by $\mathbf{b}^T \mathbf{L}(\lambda) = \mathbf{0}$, and $\mathbf{L}_{,\lambda}$ denotes $\partial \mathbf{L}/\partial \lambda$. (In this relation, it is noted that $\partial C/\partial \lambda = -i(\partial C/\partial \kappa)/2u$.) The eigenvectors $\mathbf{a}_s$ and $\mathbf{b}_s$ are determined by direct computation, by assigning one element (of $\mathbf{a}_s$ and $\mathbf{b}_s$) the value $1 + i\,0$ and solving the resultant linear equation systems. This sequence is continued until $|\lambda_{s+1} - \lambda_s| < 10^{-10}$.

All results in the following have been obtained using 50 finite elements ($N_e = 50$). This number is based on the convergence study given in Appendix A, from where it is judged that $N_e = 50$ gives sufficiently accurate results. The critical flow speeds given in the following have been determined using the bisection method.

It is remarked that the model and the corresponding numerical results do not need the inclusion of material damping to make sense, due to the presence of fluid damping. Accordingly, while we keep the material damping term in the energy considerations to follow (in Sect. 5), for the sake of completeness, we ignore it (i.e. set $\sigma^* = 0$ in (7)) in all the numerical examples to follow, to stay in line with the examples of [2].

4 Stability analysis

4.1 The approximation of Argentina and Mahadevan

In this subsection, we will investigate how the eigenvalues λ depend on the flow speed u by the approximation employed by Argentina and Mahadevan [2] which, again, consists of the terms in the first line of (7). For the discretized model, it is the terms in (13) exclusive of the terms in the last pair of curly brackets, i.e. exclusive of $\rho u \{2\mathbf{C} + u\mathbf{G}\}$.

Figures 3a, b show the real and imaginary parts of the eigenvalues for the quasi-steady approximation, $C(\kappa) \equiv 1 - i\,0$. Shown are the first six eigenvalues, $\lambda_j = \alpha_j + i\omega_j$, $j = 1, \ldots, 6$, $\omega_1 < \omega_2 < \cdots < \omega_6$, and their complex conjugates, $\lambda_j^* = \alpha_j - i\omega_j$. (Higher-order eigenvalues λ_j, $j > 6$, remain stable and are thus not included in the figures.) The eigenvalues with positive imaginary parts are drawn with full lines, while those with negative imaginary parts are drawn with broken lines. (This plotting style is adopted in all similar eigenvalue plots in the remainder of the paper.) With $C(\kappa) \equiv 1 - i\,0$, all matrices in (13) are real and accordingly, the eigenvalues occur in complex conjugate pairs, $\lambda = \alpha \pm i\,\omega$. This is clear from the symmetry about the $\omega = 0$ axis in Fig. 3b, and from the coincidence of the real parts in Fig. 3a, in the sense that the broken lines cannot be seen as they are coinciding with the full lines. It will be seen later that when $C(\kappa)$ takes complex values, the eigenvalues will still appear in complex conjugate pairs, due to the property expressed by (12). (It is thus not necessary, actually, to plot the eigenvalues with negative imaginary parts, as well as those with positive imaginary parts, but it is done nonetheless as a check of correctness.)

Figure 3a shows that the real part of the leading eigenvalue[1] (the eigenvalue with the largest real part $\alpha_* = Re(\lambda_*)$) crosses the line $\alpha = 0$ at the critical flow speed $u_c = 23.95$. The corresponding flutter frequency is $\omega_c = 22.18$. This frequency is associated with the first eigenvalue branch λ_1, that is, the branch that for $u = 0$ starts out as the first (lowest) eigenfrequency ω_1. However, at the critical flow speed, the critical eigenvalue branch is almost coinciding with the second eigenvalue branch λ_2. By 'almost' is meant that coincidence is not realized, due to the presence of fluid damping. Hence, in the quasi-steady case, the flutter motion is 'close to' coupled-mode flutter, yet it is not 'true' coupled-mode flutter, as the coupling between first and second eigenvalue branches is not complete. It is noted that if the damping matrix in (13) is proportional to the mass matrix (or equivalently, if the damping force coefficient (multiplying $\partial \eta/\partial \tau$) in (7) is proportional to the inertia force coefficient (multiplying $\partial^2 \eta/\partial \tau^2$), then the flutter instability will be 'true' coupled-mode flutter [28, p. 126]. As (7) shows, this is not so in the present case, due to the presence of the functions $f(\xi)$ and $g(\xi)$, defined by (5).

It is noted that Argentina and Mahadevan [2] use the term 'the quasi-steady approximation' for the case where, in addition to $C \equiv 1 - i\,0$, all unsteady terms in (4) are equal to zero. Using this approximation, we obtain, with $\rho = 0.2$, the critical flow speed $u_c = 23.57$. This agrees very well with the corresponding result of Argentina and Mahadevan [2]. Their results satisfy, for non-large values of ρ (say, $\rho < 1$), the approximation $u_c \approx 10.53/\sqrt{\rho}$ which, with $\rho = 0.2$, gives $u_c \approx 23.55$. In this paper, we will use the term 'the quasi-steady approximation' to refer just to the simplification $C = 1 - i\,0$.

Figure 4a shows the flutter oscillations at the onset of instability, at the critical flow speed $u_c = 23.95$, for the case $\rho = 0.2$ and $C(\kappa) \equiv 1 - i\,0$. The time step between the curves is $\Delta \tau = \pi/8\omega_c$. Figure 4b shows the

---

[1] It is emphasized, again, that all eigenvalues appear in complex conjugate pairs. Thus, by an 'eigenvalue' is really meant a pair of complex conjugate eigenvalues, and by an 'eigenvalue branch' is really meant a pair of branches (i.e., curves) of complex conjugate eigenvalues.
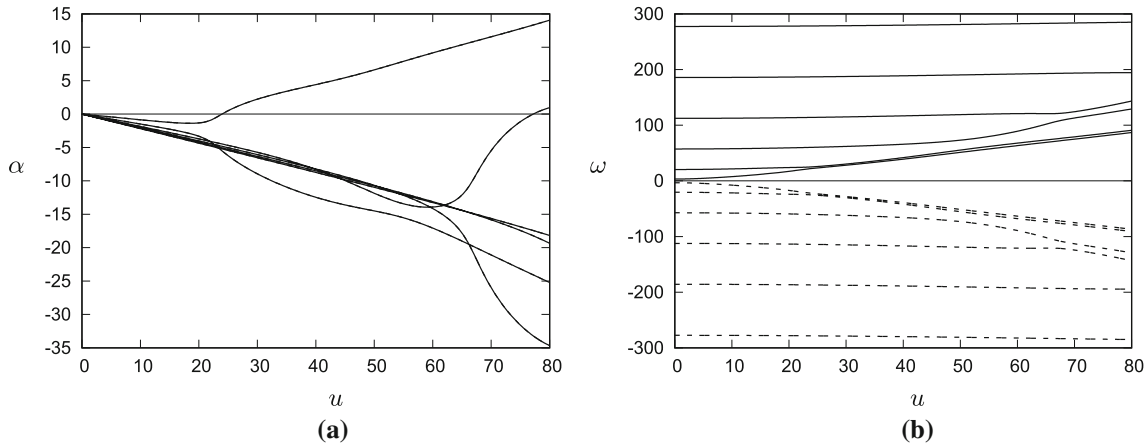
Fig. 3 **a** Real and **b** imaginary parts of the eigenvalues by a finite element discretization with 50 elements for the case $\rho = 0.2$, with $C(\kappa) \equiv 1 - \mathrm{i}0$. The critical flow speed $u_c = 23.95$. The flutter frequency $\omega_c = 22.18$. Note that the eigenvalue branches with negative imaginary parts are plotted with broken lines
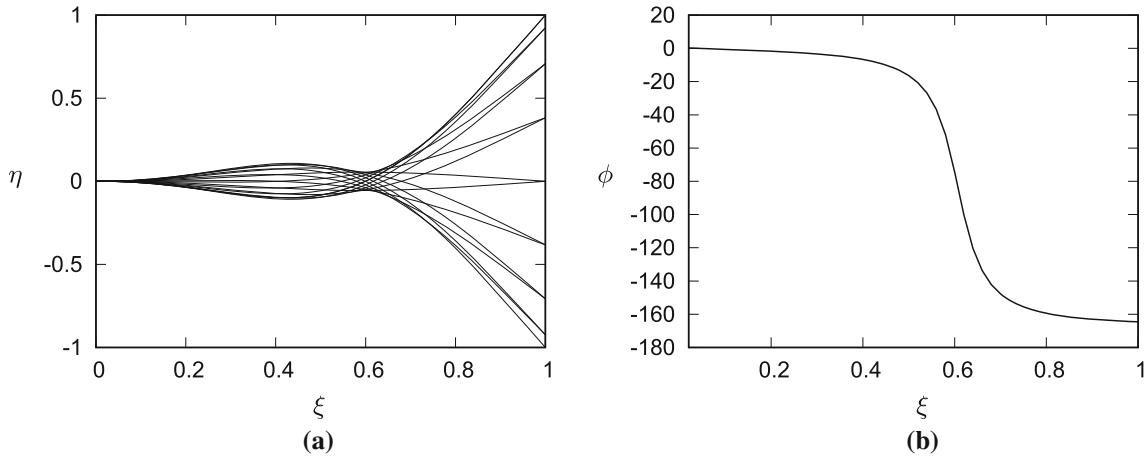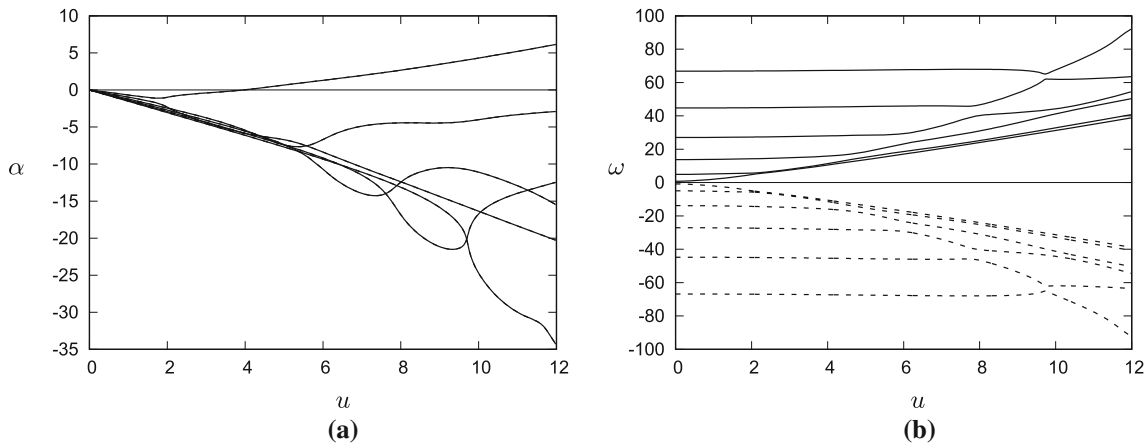

Fig. 4 **a** Flutter oscillations $\eta(\xi, \tau)$ at the onset of instability by the critical flow speed $u_c = 23.95$, for the case $\rho = 0.2$ and with $C(\kappa) \equiv 1 - \mathrm{i}0$. **b** The corresponding phase angle function $\phi(\xi)$ (in degrees)
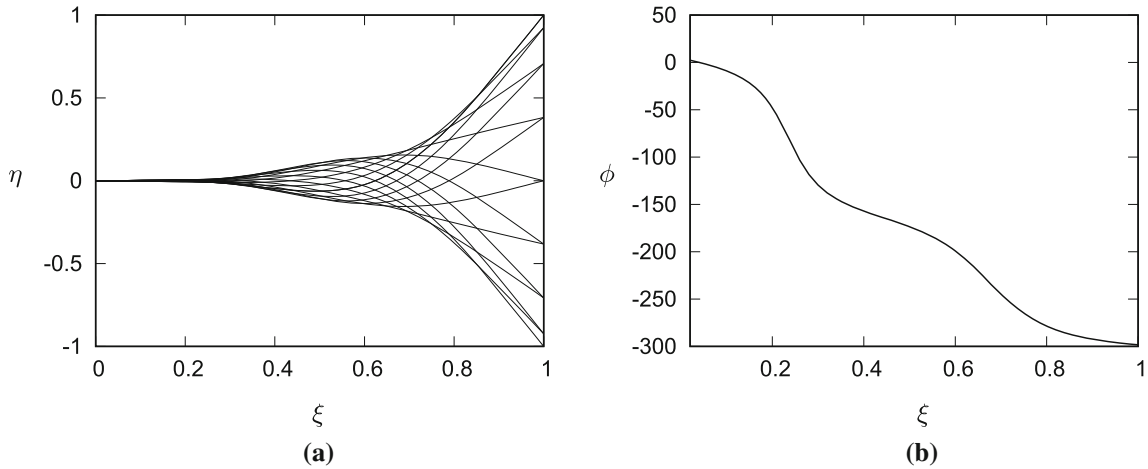
to Fig. 4a corresponding phase angle function $\phi(\xi)$. It is noted that the phase angle ϕ at element number e is evaluated as $\phi_e = \arctan(a_{I\,e}/a_{R\,e})$, where $a_{I\,e}$ and $a_{R\,e}$ are the $(2e - 1)$th elements in $\mathbf{a}_I$ and $\mathbf{a}_R$, respectively, cf. (13). In the figures, the continuous phase angle function $\phi(\xi)$ is simply interpolated between the discrete element values ϕ_e. It is noted that the phase angle gradient $\partial\phi(\xi)/\partial\xi < 0$ in the whole range $\xi \in [0, 1]$. This negative phase angle gradient results in a 'dragging' sort of motion. Considering two positions (stations) on the flag, ξ_1 and ξ_2, $0 < \xi_1 < \xi_2 < 1$, the motion at ξ_2 will always lag behind the motion at ξ_1. This dragging motion manifests itself also as a downstream traveling wave motion. (This will be discussed in more detail in Sect. 5.2.)

Thinking in terms of a classical modal (say, Bubnov–Galerkin) expansion [6, p. 58]; see also Sect. 5.2.2), and keeping the just given discussion on coupled-mode flutter in mind, it is apparent that the flutter vibrations contain components of both first and second eigenmodes. This is clear from both the vibrational shapes (Fig. 4a) and the phase shift of 180° across the 'smoothed out' nodal point (Fig. 4b). (This smoothing out is due to damping [33], which here is fluid damping.)

For the purpose of comparison, Fig. 5 shows the real and imaginary parts of the eigenvalues for the quasi-steady case ($C(\kappa) \equiv 1 - \mathrm{i}0$) with $\rho = 25$, although the quasi-steady approximation perhaps is invalid for such a large value of ρ. The real part of the leading eigenvalue crosses the line $\alpha = 0$ at the critical flow speed $u_c = 3.95$. The corresponding flutter frequency is $\omega_c = 10.37$. As in the previous case, this frequency is associated with the first eigenvalue branch λ_1 and also here, the flutter instability is 'almost' coupled-mode flutter, in the sense explained in connection with Fig. 3.

Fig. 5 **a** Real and **b** imaginary parts of the eigenvalues for the case $\rho = 25$, with $C(\kappa) \equiv 1 - \mathrm{i}\,0$. The critical flow speed $u_c = 3.95$. The flutter frequency $\omega_c = 10.37$

Fig. 6 **a** Flutter oscillations $\eta(\xi, \tau)$ at the onset of instability by $u_c = 3.95$, for the case $\rho = 25$ and with $C(\kappa) = 1 - \mathrm{i}0$. **b** The corresponding phase angle function $\phi(\xi)$ (in degrees)
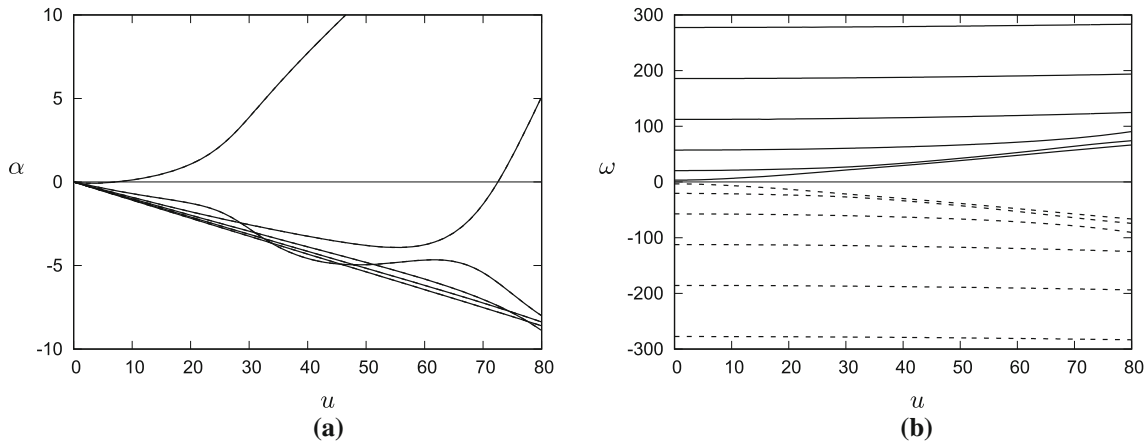
Figure 6a shows the flutter oscillations at the critical flow speed, $u_c = 3.95$, for this case ($\rho = 25$, $C(\kappa) \equiv 1 - \mathrm{i}\,0$). It is noted that the upstream quarter-part of the flag hardly vibrates at all, relative to the downstream half-part.

The to Fig. 6a corresponding phase angle function is shown in Fig. 6b. It is noted that the negative gradient of the phase angle function is very large in this case. Alone in the range $0 < \xi \lessapprox 0.5$, there is a phase shift of approximately 180°, and then one of approximately 120° in $0.5 \lessapprox \xi < 1$.
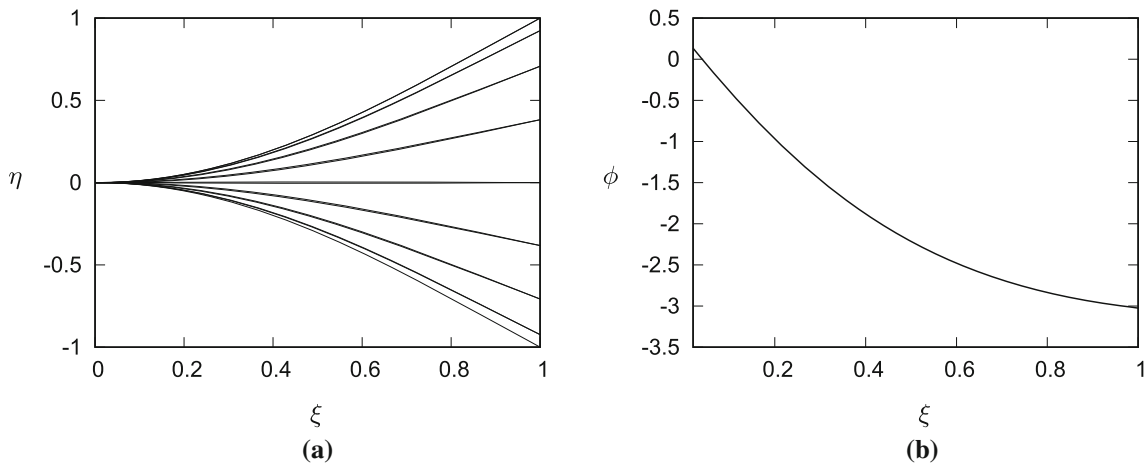
Figures 7a, b show the real and imaginary parts of the eigenvalues, evaluated with 'proper' inclusion of the Theodorsen function $C(\kappa)$, and with (13) treated as a nonlinear eigenvalue problem. The critical flow speed is here $u_c = 7.05$. The unstable eigenvalue branch is the one that at flow speed $u = 0$ corresponds to the first eigenvalue, λ_1. At the onset of flutter, the imaginary part $\omega_c = \omega_1 = 5.06$. A second crossing of the line $\alpha = 0$ occurs at $u \approx 72.5$. This eigenvalue branch corresponds, at $u = 0$, to the third eigenvalue, λ_3. At the crossing, the imaginary part of this branch takes the value $\omega = 81.2$.

Figure 8a shows the flutter oscillations at the onset of instability, at the critical flow speed $u_c = 7.05$, for the case $\rho = 0.2$ with the proper value of $C(\kappa)$. Thinking again in terms of a (Galerkin) modal expansion, it is apparent that the vibrations are here dominated by the first, fundamental eigenmode. Figure 8b shows the to Fig. 8a corresponding phase angle function $\phi(\xi)$. Comparing with Fig. 4b, we have again that the phase angle gradient $\partial\phi(\xi)/\partial\xi < 0$ in the whole range $\xi \in [0, 1]$, but now the value of $-\partial\phi(\xi)/\partial\xi$ is, in average, much smaller.

Fig. 7 **a** Real and **b** imaginary parts of the eigenvalues for the case $\rho = 0.2$, evaluated with proper inclusion of $C(\kappa)$. The critical flow speed $u_c = 7.05$. The flutter frequency $\omega_c = 5.06$

Fig. 8 **a** Flutter oscillations $\eta(\xi, \tau)$ at the onset of instability by the critical flow speed $u_c = 7.05$, for the case $\rho = 0.2$ and with proper inclusion of the Theodorsen function $C(\kappa)$. **b** The corresponding phase angle function $\phi(\xi)$ (in degrees)

Figure 9 shows the real and imaginary parts of the eigenvalues for the case with mass ratio parameter $\rho = 25$ and again with the 'correct' evaluation of the Theodorsen function $C(\kappa)$. The critical flow speed is $u_c = 2.82$, with corresponding flutter frequency $\omega_c = 5.16$. Also here, the unstable eigenvalue branch is the one that at flow speed $u = 0$ corresponds to the first eigenvalue, λ_1. A second crossing occurs at $u \approx 11.2$.

Figure 10a shows the flutter oscillations for the case $\rho = 25$, evaluated with the proper value of $C(\kappa)$. The corresponding phase angle function $\phi(\xi)$ is shown in Fig. 10b. It is interesting to note that both the flutter oscillations and the phase angle function are similar to those shown in Fig. 4. An explanation may be found by returning to Fig. 9b, where it will be seen that the two lowest eigenfrequencies ω_1 and ω_2 are in close proximity at $u = u_c$, just as they are by the quasi-steady approximation with $\rho = 0.2$ (Fig. 3b).

Since it is found that the critical flow speed is reduced significantly for the equation of motion of Argentina and Mahadevan [2] when the Theodorsen function is included, it is natural to ask what happens if the sign of the argument of the Theodorsen function, the wake wavenumber κ, is changed? If this is done for the case $\rho = 0.2$, it is found that the critical flow speed increases to $u_c \approx 67.0$. It is noted that this value appears to be close to the critical value ($u_c = 66$) identified in [2] as the critical one. Similarly, for $\rho = 25$ the critical flow speed changes to $u = 6.60$. This value agrees with the one that in [2] is identified as the critical one.

The energy analysis of Sect. 5.3 will fully clarify the effect of the Theodorsen function on the stability limit and clarify why a positive value of κ has a destabilizing effect and a negative value a stabilizing effect.

In relation to the significance of the sign of κ, it is remarked that in the paper [24], which is based on the model of Argentina and Mahadevan [2], a time dependence in the form $\exp(-i\omega\tau)$ is employed (see their
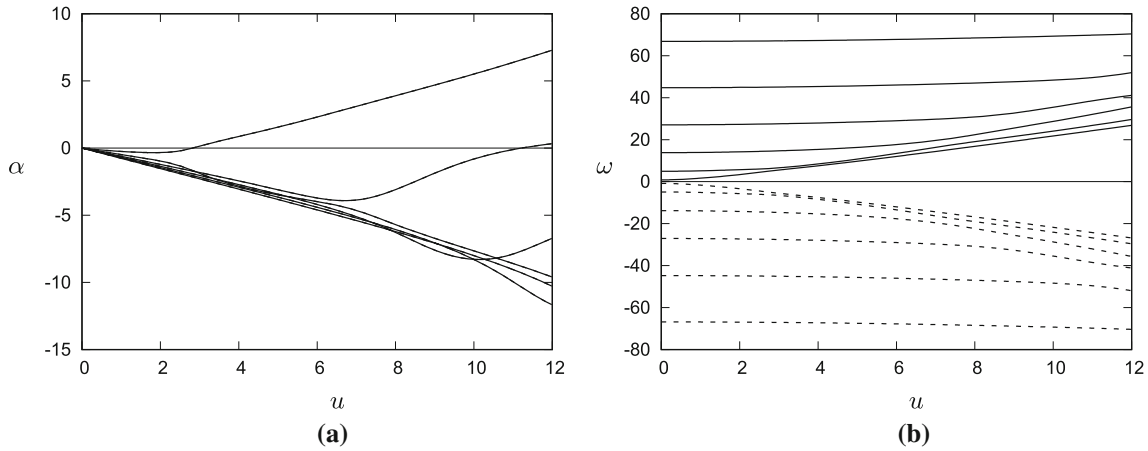
Fig. 9 a Real and **b** imaginary parts of the eigenvalues for the case $\rho = 25$, evaluated with proper inclusion of $C(\kappa)$. The critical flow speed $u_c = 2.82$. The flutter frequency $\omega_c = 5.16$
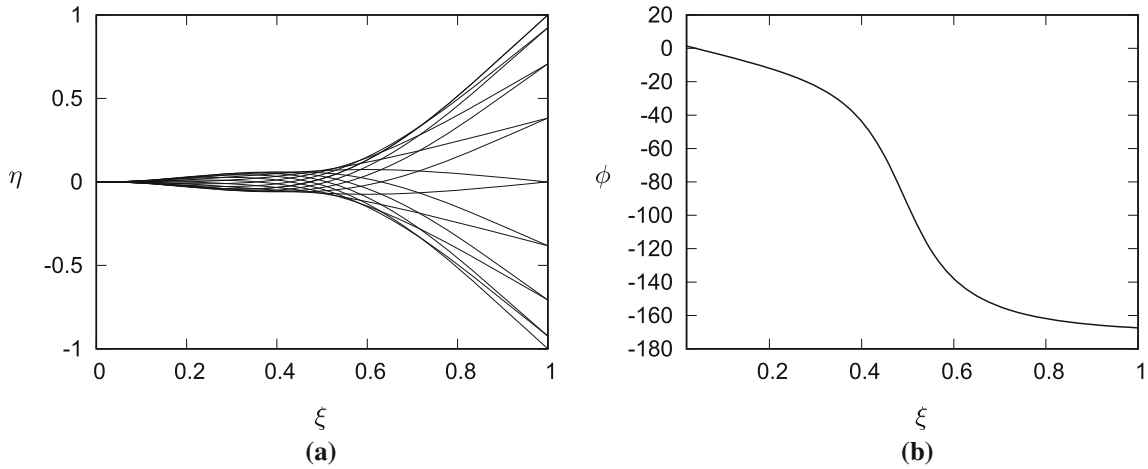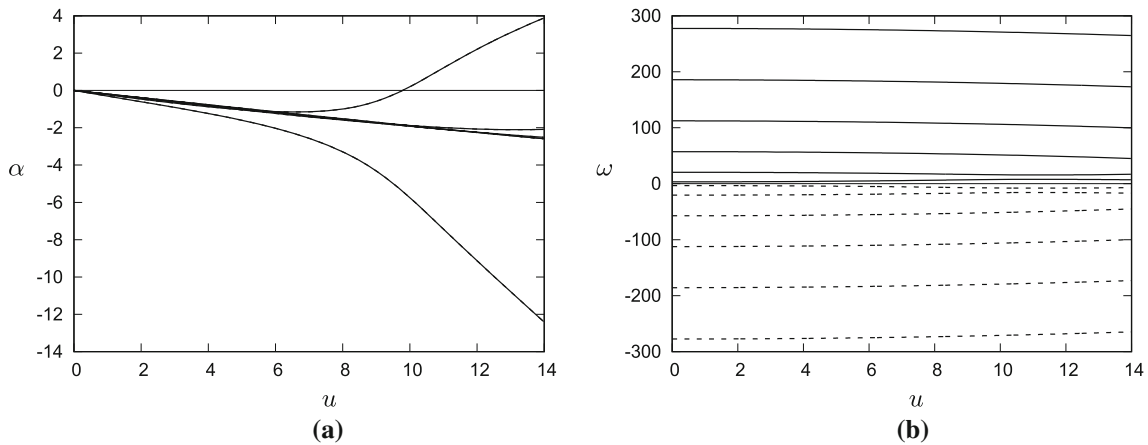

Fig. 10 a Flutter oscillations at the onset of instability by $u_c = 2.82$, for the case $\rho = 25$ and with proper inclusion of $C(\kappa)$. **b** The corresponding phase angle function $\phi(\xi)$ (in degrees)

Eq. (3.5), and consider then the inverse transform which gives $\eta(\xi, \tau)$ (here using our notation)); however, the vorticity distribution function which enters the Theodorsen functional (cf. [2] for details) is assumed to have a time dependence in the form $\exp(i\omega\tau)$ (see their Eq. (3.8)). This gives, in effect, a change of sign of the argument of the Theodorsen function, just as we have considered here. In the paper [23], a sign error is introduced (compare their Eqs. (9), (31), and (32)) which implies exactly the same effect. It will be shown in Sect. 5 that flutter occurs in the form of a downstream traveling wave. The vortex sheet, representing the vorticity shed from the trailing edge of the flag, clearly also travels downstream. But if the time dependence of the flag motion is taken as $\exp(-i\omega\tau)$ and that of the vorticity distribution of the wake corresponding to this motion as $\exp(i\omega\tau)$, this will, in effect, amount to a wake (vortex sheet) traveling against the flow, which clearly is meaningless.
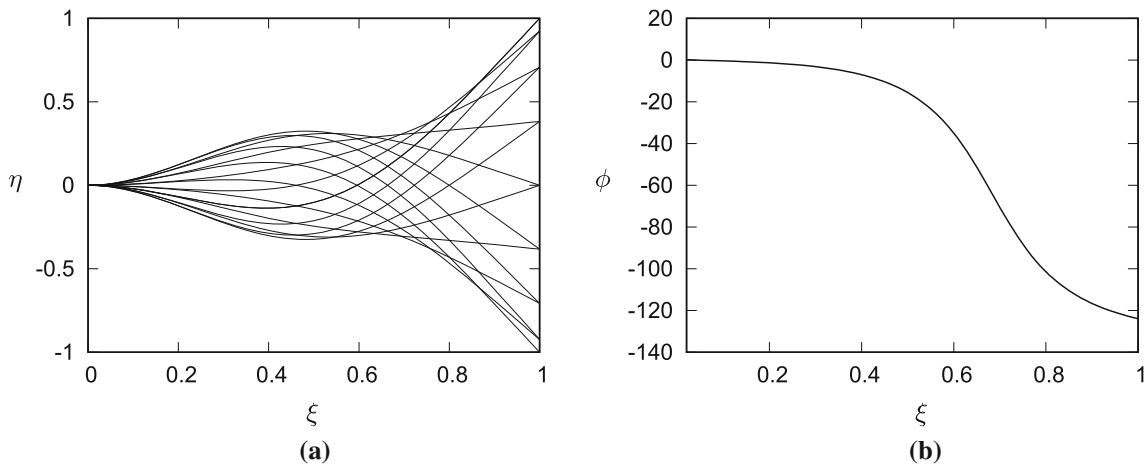
4.2 The influence of the Coriolis and centrifugal terms

In the following, we will investigate how the two 'new' terms in (7), the Coriolis force term $2\rho u g \partial^2 \eta / \partial \tau \partial \xi$ and the Centrifugal force term $\rho u^2 g \partial^2 \eta / \partial \xi^2$, affect the eigenvalues λ as functions of the flow speed u.

Figures 11a, b show the real and imaginary parts of the eigenvalues, evaluated with a 'proper' inclusion of the Theodorsen function $C(\kappa)$, for $\rho = 0.2$. The critical flow speed $u_c = 9.78$, with flutter frequency $\omega_c = 16.09$, by the branch which at $u = 0$ starts as the second eigenvalue. With the quasi-steady approximation $C = 1 - i0$,

Fig. 11 a Real and **b** imaginary parts of the eigenvalues for the case $\rho = 0.2$, evaluated with inclusion of the Coriolis and centrifugal force terms and with proper inclusion of $C(\kappa)$. The critical flow speed $u_c = 9.78$. The flutter frequency $\omega_c = 16.09$
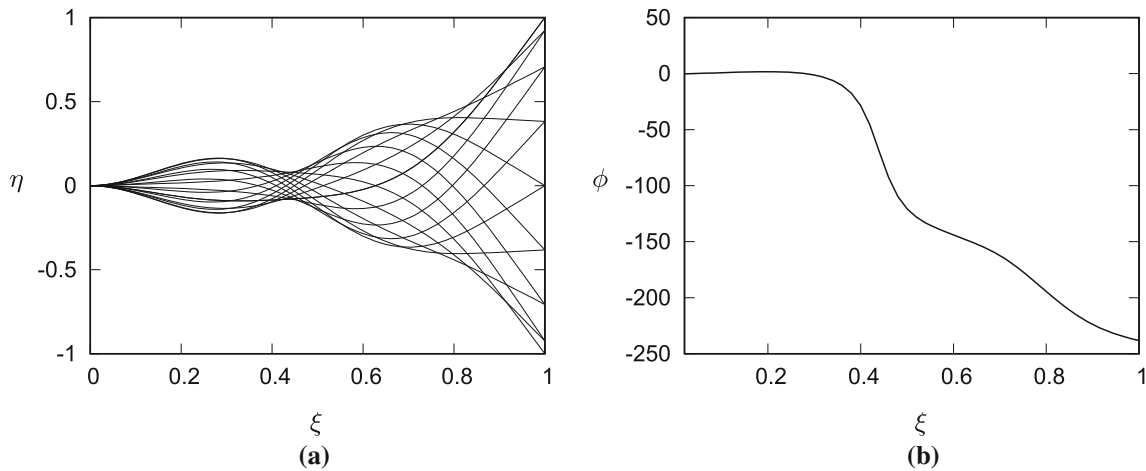

Fig. 12 a Flutter oscillations at the onset of instability by $u_c = 9.78$, for the case $\rho = 0.2$, evaluated with inclusion of the Coriolis and centrifugal force terms and with proper inclusion of $C(\kappa)$. **b** The corresponding phase angle function $\phi(\xi)$ (in degrees)

the course of the eigenvalues remains basically unchanged; however, the critical flow speed increases to $u_c = 10.13$, while the flutter frequency changes to $\omega_c = 16.83$. Thus, in contrast to the approximatively 70% drop in the value of u_c by the approximation of [2], the influence of the Theodorsen function on u_c is moderate when the Coriolis and centrifugal terms are included in (4) and (7). It is noted that the critical flow speed u_c for this value of the fluid loading parameter ρ agrees well with that of Tang and Païdoussis [36,37], who found $u_c = 9.95$ based on a different method. This moderate influence of the Theodorsen function is also in qualitative agreement with an example in Hodges and Pierce [15, pp. 143,154], who, for a two degrees of freedom wing model, show that, relative to the quasi-steady approximation $C = 1 - i0$, when the Theodorsen function is properly included, the change in the critical flow speed is less than 20%.

Figure 12a shows the flutter oscillations at the critical flow speed, $u_c = 9.78$, for this case ($\rho = 0.2$). Comparing with Figs. 4 and 8, it is noted that the second eigenmode is dominating in this case. The to Fig. 12a corresponding phase angle function is shown in Fig. 12b. It is noted that the gradient here is smaller than in Fig. 4b (but much larger than in Fig. 8b).

Figure 13a shows the flutter oscillations at the critical flow speed, $u_c = 11.90$, for the case $\rho = 0.5$. Comparing with Fig. 12, it is noted that the presence of the third eigenmode can be seen in this case. In this relation, the flutter frequency $\omega_c = 31.88$ is here by the branch which at $u = 0$ starts as the third eigenvalue. It is interesting to note that when the quasi-static approximation $C = 1 - i0$ is used in this case, the critical flow speed does not change within four significant digits. The flutter frequency changes to $\omega_c = 33.71$. The

Fig. 13 a Flutter oscillations at the onset of instability by $u_c = 11.90$, for the case $\rho = 0.5$, evaluated with inclusion of the Coriolis and centrifugal force terms and with proper inclusion of $C(\kappa)$. The flutter frequency $\omega_c = 31.88$. **b** The corresponding phase angle function $\phi(\xi)$ (in degrees)
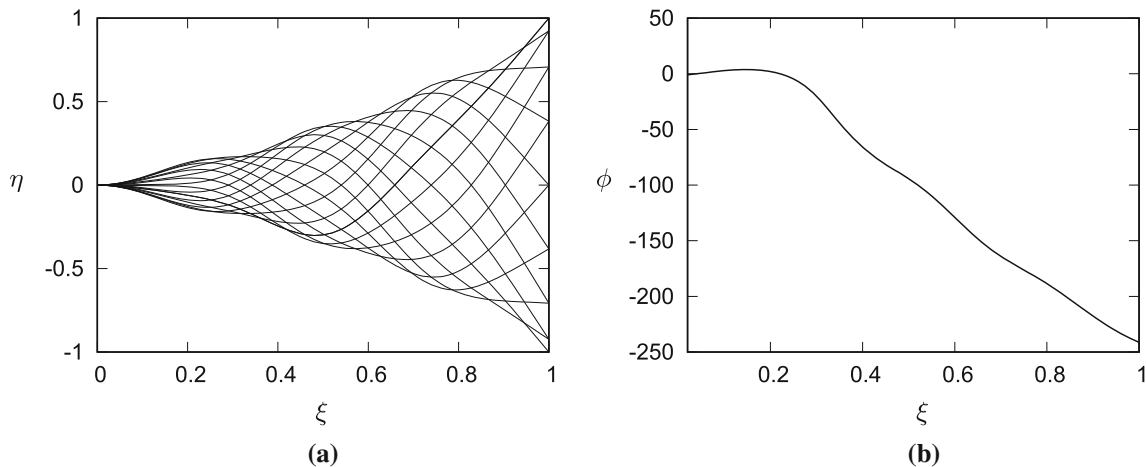
Fig. 14 a Flutter oscillations at the onset of instability by $u_c = 10.32$, for the case $\rho = 2$, evaluated with inclusion of the Coriolis and centrifugal force terms and with proper inclusion of $C(\kappa)$. The flutter frequency $\omega_c = 42.54$. **b** The corresponding phase angle function $\phi(\xi)$ (in degrees)

phase angle function corresponding to Fig. 13a is shown in Fig. 13b. The large gradient and the very large phase shift between $\xi = 0$ and $\xi = 1$ should be noticed.

Flutter oscillation and phase angle plots for the case $\rho = 2$ are shown in Fig. 14. Here, the critical flow speed $u_c = 10.32$, and flutter takes place at the frequency $\omega_c = 42.54$. This is again by the branch which at $u = 0$ starts as the third eigenvalue. It is noted that if the quasi-static approximation $C = 1 - i0$ is used in this case, the critical flow speed changes to $u_c = 12.97$ and the flutter frequency to $\omega_c = 72.83$. Here, the critical eigenvalue is actually associated with the branch which at $u = 0$ starts as the fourth eigenvalue.

To recapitulate the main finding of this section, when the Coriolis and centrifugal force terms are included in (7) (and in (13)), the influence of the Theodorsen function (or in physical terms, the influence of the wake) on the critical flow speed is greatly reduced. It is noted also that the evolution of the flutter oscillations by increasing value of ρ, where higher and higher eigenmodes come into play at a pace much higher than by the approximation of Argentina and Mahadevan [2], is in agreement with results based on other methods, such as those of Tang and Païdoussis [36,37], who employed the discrete vortex method, and those of Watanabe et al. [41], who employed a traditional CFD (computational fluid dynamics) approach with a finite difference discretization of the Navier–Stokes equations, as well as a potential flow model based on the theory of Küssner and Schwartz (cf. [5,14]). So is the finding that the changes in the numerical magnitude of the critical flow speed u_c with changing values of ρ are relatively small, at least for the range of ρ-values considered here.

5 Energy considerations

Argentina and Mahadevan [2] and Manela and Howe [23] claim that the critical flow speed is lower for the quasi-steady approximation than for the case where the Theodorsen function is properly included, while we have found the opposite to be the case. In order to understand this, and also to obtain a better understanding of the mechanism behind the flutter instability, we will investigate the energetics of the fluid–structure interaction in the present system.

5.1 General equations

Multiplication of the equation of motion (7) by the lateral flag velocity $\partial \eta / \partial \tau$, followed by integration over the flag surface, $0 \leq \xi \leq 1$, gives a power (rate of work) balance equation. Integrating this equation over time, say from $\tau = \tau_1$ to τ_2, gives an energy balance equation. Writing (7) in the operator form $\mathfrak{L}(\eta) = 0$, we have

$$\int_{\tau_1}^{\tau_2} \int_0^1 \frac{\partial \eta}{\partial \tau} \mathfrak{L}(\eta) \mathrm{d}\xi \mathrm{d}\tau = 0. \tag{15}$$

Inserting (7), this equation can be rewritten as

$$
\begin{aligned}
[\Delta E]_{\tau_1}^{\tau_2} = [\Delta T + \Delta V]_{\tau_1}^{\tau_2} \\
= \int_{\tau_1}^{\tau_2} \left[-\int_0^1 \sigma^* \left(\frac{\partial^3 \eta}{\partial \xi^2 \partial \tau} \right)^2 \mathrm{d}\xi - \rho u \int_0^1 C(\kappa) f(\xi) \left\{ \left(\frac{\partial \eta}{\partial \tau} \right)^2 + u \frac{\partial \eta}{\partial \tau} \frac{\partial \eta}{\partial \xi} \right\} \mathrm{d}\xi \right] \mathrm{d}\tau \\
- \int_{\tau_1}^{\tau_2} \int_0^1 \rho u g(\xi) \frac{\partial \eta}{\partial \tau} \left\{ 2 \frac{\partial^2 \eta}{\partial \tau \partial \xi} + u \frac{\partial^2 \eta}{\partial \xi^2} \right\} \mathrm{d}\xi \mathrm{d}\tau,
\end{aligned}
\tag{16}
$$

where

$$T = \tfrac{1}{2} \int_0^1 \{1 + \rho g(\xi)\} \left(\frac{\partial \eta}{\partial \tau} \right)^2 \mathrm{d}\xi \tag{17}$$

is the kinetic energy of the flag, including the extra contribution due to the added fluid mass, and

$$V = \tfrac{1}{2} \int_0^1 \left(\frac{\partial^2 \eta}{\partial \xi^2} \right)^2 \mathrm{d}x \tag{18}$$

is the potential energy of the flag. $[\Delta E]_{\tau_1}^{\tau_2}$ thus indicates the change in mechanical energy from time $\tau = \tau_1$ to time $\tau = \tau_2$.

In the following, we will assume that the time interval $[\tau_1, \tau_2]$ is coinciding with one period of oscillation, say, $\tau_1 = 0$ and $\tau_2 = 2\pi/\omega$, such that the deflection of the flag at time $\tau = \tau_2$ coincides with the deflection at $\tau = \tau_1$.

The first term in the right-hand side of (16) represents the energy dissipated by internal (flag material) damping. Since the integrand is positive definite and there is a minus in front of the term, it is clear that this term reduces the mechanical energy in each period of oscillation.

First, we ignore the terms in the last line of (16) and consider Argentina and Mahadevan's [2] example for the case where $\rho \to 0$ and $u \to \infty$ in such a way that the fluid force multiplier ρu^2 remains finite. Equation (10) then gives that $\kappa \to 0$ and, as shown in Appendix B, the Theodorsen function

$$C(\kappa) \sim 1 - (\pi/2)\kappa - \mathrm{i}(\ln 2 + 1 - \gamma)\kappa \tag{19}$$

in this limit. (Here, γ is Euler's constant, $\gamma = 0.5771\ldots$ and $\ln 2 + 1 - \gamma \approx 1.1160$.) We will here first consider the limit case $\lim_{\kappa \to 0} C(\kappa) = 1 - \mathrm{i}0$, the quasi-steady approximation, which is precisely satisfied in the case of steady flow [2]. Since the function $f(\xi) > 0$ for all $\xi \in [0, 1]$, cf. (5), the second term on the right-hand side of (16) (proportional to ρu) thus acts as a dissipative term, too.

Flutter motion at the threshold of instability is characterized by $[\Delta E]_0^{2\pi/\omega} = 0$ and unstable flutter oscillations by $[\Delta E]_0^{2\pi/\omega} > 0$. Both of these conditions can be satisfied only if the third term on the right-hand side of (16) (proportional to ρu^2) is positive. This is realized only if $\partial \eta/\partial \tau$ and $\partial \eta/\partial \xi$ have opposite signs over most part of the domain $\xi \in [0, 1]$, and over most part of the vibrational period $0 \leq \tau \leq \pi/\omega$. How this is realized is discussed in detail in Sect. 5.2.

Consider next the influence of the Coriolis force term and the centrifugal force term, that is, the two 'new' terms represented by the last line of (16). Integration by parts of the Coriolis force term (the first term) gives, with use of the boundary conditions and the fact that $g(0) = g(1) = 0$,

$$2 \int_0^1 g(\xi) \frac{\partial \eta}{\partial \tau} \frac{\partial^2 \eta}{\partial \tau \partial \xi} d\xi = - \int_0^1 \frac{dg(\xi)}{d\xi} \left(\frac{\partial \eta}{\partial \tau} \right)^2 d\xi. \tag{20}$$

It will be shown in Sect. 5.2.1 that the integral on the left-hand side actually is positive (or equivalently, that the one on the right-hand side is negative) and thus that the Coriolis force term acts as a dissipative term.

Considering now the last term, the centrifugal force term, it is seen that is order for this term to act as an energy source, which sends energy from the flow into the fluttering flag, it is necessary that $\partial \eta/\partial \tau$ and $\partial^2 \eta/\partial \xi^2$ have opposite signs over most part of the domain $\xi \in [0, 1]$, and over most part of the vibrational period $0 \leq \tau \leq \pi/\omega$. It will be shown in Sect. 5.2.1 that this is actually not the case and thus that it is the last term in the second line of (16) that acts as the main energy source.

It is of interest at this point to compare the present case with that of a cantilevered fluid-conveying pipe [18,26,34], for which the 'fluid force' terms correspond just to the 'new' Coriolis and centrifugal force terms in (16), but without the presence of the function $g(\xi)$. That is to say, the fluid forces appear in the form $\rho u \left\{ \partial^2 \eta/\partial \tau \partial \xi + u \partial^2 \eta/\partial \xi^2 \right\}$. Using integration by parts for the spatial integral in (16), the energy delivered to the structural vibrations by these forces during one period of oscillation is given by $-\rho u \int_0^{2\pi/\omega} [\partial \eta/\partial \tau \{\partial \eta/\partial \tau + u \partial \eta/\partial \xi\}]_{\xi=1} d\tau$. Since the first term, $(\partial \eta/\partial \tau)^2$, clearly is positive definite, flutter is realized only if $\partial \eta/\partial \tau$ and $\partial \eta/\partial \xi$, evaluated at the free column end, $\xi = 1$, have opposite signs over most part of each vibrational period. In other words, for the fluid-conveying pipe, the energy delivered to the vibrating structure from the flowing fluid is dependent on the phase difference between $\partial \eta/\partial \tau$ and $\partial \eta/\partial \xi$ at the free end only, whereas for the flag, it is dependent on this phase difference (between $\partial \eta/\partial \tau$ and $\partial \eta/\partial \xi$) over the whole domain $0 \leq \xi \leq 1$.

5.2 Influence of the phase angle distribution on the energy balance

5.2.1 Representation with continuous phase angle function

In order to get a more detailed understanding of how flutter is realized by a flapping flag, we will consider vibrations just at the threshold of flutter instability, at the critical flow speed $u = u_c$, where steady-state oscillations occur, with $[\Delta E]_0^{2\pi/\omega} = 0$. These vibrations can be expressed as [33]

$$\eta(\xi, \tau) = A(\xi) \cos(\omega_c \tau + \phi(\xi)), \tag{21}$$

where $A(\xi)$ is an amplitude function, $\phi(\xi)$ a is phase angle function and ω_c is the flutter frequency.

Consider first the case $C(\kappa) \equiv 1 - \mathrm{i}\, 0$. Inserting (21) into (16) and evaluating the time integrals, we obtain

$$\begin{aligned}
[\Delta E]_0^{2\pi/\omega_c} = &-\pi \omega_c \int_0^1 \sigma^* \left[\left\{ \frac{d^2 A}{d\xi^2} - A \frac{d^2 \phi}{d\xi^2} \right\}^2 + \left\{ 2 \frac{dA}{d\xi} \frac{d\phi}{d\xi} + A \frac{d^2 \phi}{d\xi^2} \right\}^2 \right] d\xi \\
&- \rho u_c \pi \left[\omega_c \int_0^1 f(\xi) A^2(\xi) d\xi + u_c \int_0^1 f(\xi) A^2(\xi) \frac{d\phi(\xi)}{d\xi} d\xi \right] \\
&- \rho u_c \pi \left[2\omega_c \int_0^1 g(\xi) A(\xi) \frac{dA(\xi)}{d\xi} d\xi + u_c \int_0^1 g(\xi) \left\{ 2A(\xi) \frac{dA(\xi)}{d\xi} \frac{d\phi(\xi)}{d\xi} + A^2(\xi) \frac{d^2 \phi(\xi)}{d\xi^2} \right\} d\xi \right].
\end{aligned} \tag{22}$$

Here, the terms in the last line correspond to the terms in the last line of (7). Assuming first that these terms are zero, then, in order to satisfy $[\Delta E]_0^{2\pi/\omega} = 0$, it is necessary that the integral

$$\int_0^1 f(\xi)A^2(\xi)\frac{d\phi(\xi)}{d\xi}d\xi < 0, \tag{23}$$

since all the proceeding integrals are positive definite (and there is a minus in front of any term). Since $f(\xi)$ is positive definite, the phase angle gradient $\partial\phi(\xi)/\partial\xi$ needs to be negative over the most part of $\xi \in [0, 1]$. The results of Figs. 4, 6, 8, and 10 indicate that this is indeed the case.

Consider next the influence of the Coriolis force term and the centrifugal force term, that is, the 'new' terms represented by the last line of (22). Integration by parts of the Coriolis force term gives, with use of the boundary conditions and the fact that $g(0) = g(1) = 0$,

$$2\int_0^1 g(\xi)A(\xi)\frac{dA(\xi)}{d\xi}d\xi = -\int_0^1 \frac{dg(\xi)}{d\xi}A^2(\xi)d\xi. \tag{24}$$

It is noted that $dg(\xi)/d\xi > 0$ for $0 < \xi < 1/2$ and $dg(\xi)/d\xi < 0$ for $1/2 < \xi < 1$, as is evident from Fig. 2b, and in light of Figs. 12, 13 and 14, we can assume that $d\phi/d\xi < 0$ for all $\xi \in [0, 1]$. Noting the symmetry of $g(\xi)$ (cf. Fig. 2b), it follows that the integral on the left-hand side of (24) is positive if $\int_{1/2}^1 A^2(\xi)d\xi > \int_0^{1/2} A^2(\xi)d\xi$ and negative otherwise. With the present clamped-free boundary conditions, and as the flutter vibrations shown in Figs. 12, 13 and 14 also indicate, this will be so, that is, (24) will be positive. Thus, the Coriolis force term will act as a dissipative term.

Integration by parts of the first of the two centrifugal force terms gives, with use of the boundary conditions (and $g(0) = g(1) = 0$),

$$2\int_0^1 g(\xi)A(\xi)\frac{\partial A(\xi)}{\partial\xi}\frac{\partial\phi(\xi)}{\partial\xi}d\xi = -\int_0^1 g(\xi)A^2(\xi)\frac{d^2\phi(\xi)}{d\xi^2}d\xi - \int_0^1 \frac{dg(\xi)}{d\xi}A^2(\xi)\frac{d\phi(\xi)}{d\xi}d\xi. \tag{25}$$

Adding the very last term of (22) to this result, only the last term in the right-hand side of (25) remains. For this term, it is noted again that $dg(\xi)/d\xi < 0$ for $1/2 < \xi < 1$, and in this domain $A(\xi)$ is largest. Since $d\phi/d\xi < 0$ for all $\xi \in [0, 1]$, it follows that this term will not contribute significantly to the flutter instability. This is supported by the numerical results of Sect. 4.2, which show that inclusion of the Coriolis and centrifugal force terms in general has a 'stabilizing effect'.

The conclusion is thus that it is mainly the term 'highlighted' in (23) that feeds energy to the fluttering flag, and this happens, again, if the phase angle gradient $\partial\phi(\xi)/\partial\xi$ is negative over the most part of $\xi \in [0, 1]$. In this relation, it is noted that the bending wavenumber k for the 'waving' flag (plate) is defined as 'minus the phase change per unit increase in distance' [11, p. 3], i.e. $k(\xi) = -\partial\phi/\partial\xi$ [21, p. 310]. The bending wave speed $c(\xi)$ is, at the flutter frequency ω_c, defined as

$$c(\xi) = \frac{\omega_c}{k(\xi)}. \tag{26}$$

This expression shows that the flutter motion is a traveling wave motion, traveling in the direction of positive ξ, just like the numerical examples in Sect. 4 indicate.

It is of interest to end this subsection with a return to a comparison with the fluid-conveying pipe. As discussed in Sect. 5.1, the fluid force terms are equivalent to the terms in the last line of (22), but without the presence of the function $g(\xi)$. Integration by parts and use of the boundary conditions gives

$$[\Delta E]_0^{2\pi/\omega_c} = -\rho u_c \pi \left[2\omega_c \int_0^1 A(\xi)\frac{dA(\xi)}{d\xi}d\xi + u_c \int_0^1 \left\{ 2A(\xi)\frac{dA(\xi)}{d\xi}\frac{d\phi(\xi)}{d\xi} + A^2(\xi)\frac{d^2\phi(\xi)}{d\xi^2} \right\} d\xi \right]$$

$$= -\rho u_c \pi \left\{ \omega_c A^2(1) + u_c A^2(1) \left[\frac{d\phi}{d\xi} \right]_{\xi=1} \right\}. \tag{27}$$

Thus, for the fluid-conveying pipe, a necessary condition for flutter is that $[d\phi/d\xi]_{\xi=1} < 0$; that is, here we have a conditions that apply only at a point (a boundary), rather than an integral condition as (23) for the flapping flag.

5.2.2 Representation by modal functions

In Sect. 4, we made reference to a modal (eigenmode) expansion, as used in a Bubnov–Galerkin discretization, and it may be of interest to consider how the influence of the phase angle distribution comes into play in the energy balance equation (16) when applying this discretization approach, by which the flag/plate deflection $\eta(\xi, \tau)$ is expanded in a series in the form [6, p. 58],

$$\eta(\xi, \tau) = \sum_{n=1}^{N} b_n f_n(\xi) \exp(\lambda \tau). \tag{28}$$

Here, $f_n(\xi)$ are the eigenmodes, or modal functions, for free (beam-like) vibrations of a cantilevered plate. These functions satisfy the boundary conditions (8). The complex constants[2] $b_n = b_{n\,R} + i b_{n\,I}$ are determined by the conditions

$$\sum_{m=1}^{N} b_m \int_0^1 \mathfrak{L}(f_m(\xi)) f_n(\xi) \mathrm{d}\xi = 0, \quad n = 1, 2, \cdots, N, \tag{29}$$

where the operator notation introduced in (15) has been used. The modal functions have the form [4, p. 382]

$$f_n(\xi) = \cosh(a_n \xi) - \cos(a_n \xi) - g_n \{\sinh(a_n \xi) - \sin(a_n \xi)\}, \tag{30}$$

where

$$a_n = \left(\frac{m}{B}\right)^{\frac{1}{4}} \omega^{\frac{1}{2}}, \quad g_n = \frac{\sinh a_n - \sin a_n}{\cosh a_n + \cos a_n}. \tag{31}$$

The coefficients (eigenvalues) a_n are the roots of the transcendental equation $\cos a_n \cosh a_n + 1 = 0$.

For the evaluation of the energy balance equation (16), we consider an expansion in the real form

$$\eta(\xi, \tau) = \sum_{n=1}^{N} A_n f_n(\xi) \cos(\omega_c \tau + \phi_n), \tag{32}$$

where $A_n = \sqrt{b_{n\,R}^2 + b_{n\,I}^2}$ and $\tan \phi_n = b_{n\,I}/b_{n\,R}$.

Analytical evaluation of the integrals in (16) with (32) inserted is not possible with the presence of the functions $f(\xi)$ and $g(\xi)$ (see (5)). It is possible only if we set $f(\xi) = g(\xi) \equiv 1$. Since these functions are positive definite, evaluation with $f(\xi) = g(\xi) \equiv 1$ is meaningful from a qualitative point of view and in the light that it gives extended analytical understanding. Thus, we obtain, with $f(\xi) = g(\xi) \equiv 1$,

$$
\begin{aligned}
[\Delta E]_0^{2\pi/\omega} = [\Delta T + \Delta V]_{\tau_1}^{\tau_2} = &-\sigma^* \pi \omega_c \sum_n a_n^4 A_n^2 \\
&-\rho u_c C \pi \omega_c \sum_n A_n^2 + \rho u_c^2 C \pi \sum_m \sum_n A_m A_n \frac{4 \sin(\phi_m - \phi_n)}{\left(\frac{a_m}{a_n}\right)^2 + (-1)^{m+n}} \\
&-\rho u_c \omega_c 2\pi \sum_n A_n^2 + \rho u_c^2 \pi \sum_m \sum_n A_m A_n \frac{4(a_m g_m - a_n g_n) \sin(\phi_m - \phi_n)}{\left(\frac{a_m}{a_n}\right)^2 - (-1)^{m+n}}.
\end{aligned}
\tag{33}
$$

The terms in the last line correspond to the terms in the last line of (22). Assuming first that these terms are zero, focussing on the fluid force terms in the second line, it is noticed that the condition $[\Delta E]_0^{2\pi/\omega} = 0$ can be satisfied if $\phi_m - \phi_n \gtrless 0$ and $(a_m/a_n)^2 + (-1)^{m+n} \gtrless 0$. Considering next the last line, the last term in this line can only be positive if $\phi_m - \phi_n \gtrless 0$ and $(a_m/a_n)^2 - (-1)^{m+n} \gtrless 0$. In other words, for both cases it is seen that different phase angles between at least some of the individual modes are necessary for flutter to take place, and individual modes that are out of phase with each other combine to form a traveling wave (e.g. [12] § 49.)

---

[2] The use of the symbols a_n and b_n in this subsection should not be confused with the elements of the right and left eigenvectors **a** and **b** used in the finite element analysis of Sect. 3.

5.3 Influence of the Theodorsen function on the energy balance

In order to understand the apparent 'destabilizing effect' of the Theodorsen function, we investigate in the following how its inclusion affects the energy balance (16). We return again to the representation (21) with a continuous phase angle function. The Theodorsen function C can be written as[3]

$$C(\kappa) = F(\kappa) - i\bar{G}(\kappa), \tag{34}$$

where F and $\bar{G}$ are real, positive definite functions. Rather than just inserting (34) into (22), it is useful to reconsider (16) in order to keep the final result in real form. Since multiplication with $-i$ corresponds to a phase shift of $-\pi/2$, we can write

$$-i\bar{G}\frac{\partial\eta}{\partial\tau}\frac{\partial\eta}{\partial\xi} = \bar{G}\frac{\partial\eta}{\partial\tau}\frac{\partial\tilde{\eta}}{\partial\xi}, \tag{35}$$

where

$$\tilde{\eta}(\xi,\tau) = A(\xi)\cos(\omega_c\tau - \pi/2 + \phi(\xi)) = A(\xi)\sin(\omega_c\tau + \phi(\xi)). \tag{36}$$

Inserting these expressions into (16) and evaluating again the time integrals, we obtain

$$
\begin{aligned}
[\Delta E]_0^{2\pi/\omega_c} = &-\pi\omega_c \int_0^1 \sigma^* \left[\left\{ \frac{d^2A}{d\xi^2} - A\frac{d^2\phi}{d\xi^2} \right\}^2 + \left\{ 2\frac{dA}{d\xi}\frac{d\phi}{d\xi} + A\frac{d^2\phi}{d\xi^2} \right\}^2 \right] d\xi \\
&- \rho u_c \pi \left[\omega_c F(\kappa) \int_0^1 f(\xi)A^2(\xi)d\xi + u_c F(\kappa)\int_0^1 f(\xi)A^2(\xi)\frac{d}{d\xi}\phi(\xi)d\xi \right] \\
&+ \rho u_c^2 \pi \bar{G}(\kappa) \int_0^1 f(\xi)A(\xi)\frac{d}{d\xi}A(\xi)d\xi \\
&- \rho u_c \pi \left[2\omega_c \int_0^1 g(\xi)A(\xi)\frac{dA(\xi)}{d\xi}d\xi + u_c \int_0^1 g(\xi)\left\{ 2A(\xi)\frac{dA(\xi)}{d\xi}\frac{d\phi(\xi)}{d\xi} + A^2(\xi)\frac{d\phi(\xi)}{d\xi} \right\} d\xi \right].
\end{aligned} \tag{37}
$$

It is noted that the real part $F(\kappa) \in [\frac{1}{2}, 1]$, with $F \to 1$ for $\kappa \to 0$, and that $F \to \frac{1}{2}$ for $\kappa \to \infty$, cf. Appendix B. However, $F(\kappa)$ acts as a multiplier to both of the two 'competing' fluid force terms in the second line; in other words, they are both reduced by the same factor (relative to $\max_\kappa F = 1$). Equation (37) thus shows that, in the absence of internal damping ($\sigma^* = 0$), and if $\bar{G}(\kappa) = 0$ as well, a change in the magnitude of $F(\kappa)$ will have no effect on the critical flow speed.

Consider now the term proportional to $\bar{G}$. Equivalent to (24), integration by parts and use of the boundary conditions, and the fact that $f(1) = 0$, gives

$$\int_0^1 f(\xi)A(\xi)\frac{d}{d\xi}A(\xi)d\xi = -\frac{1}{2}\int_0^1 \frac{df(\xi)}{d\xi}A^2(\xi)d\xi. \tag{38}$$

It is easy to show, and it is also evident from Fig. 2, that $df(\xi)/d\xi < 0$ for all $\xi \in [0, 1]$. Thus, the term proportional to $\bar{G}$ is positive definite. This means that a small positive value of $\bar{G}$ will *lower* the critical flow speed u_c relative to its value for $\bar{G} = 0$. It is noted that

$$C(\kappa) \sim 1 - \frac{\pi}{2}\kappa - i(\ln 2 + 1 - \gamma)\kappa, \text{ that is, } F(\kappa) \sim 1 - \frac{\pi}{2}\kappa, \quad \bar{G}(\kappa) \sim (\ln 2 + 1 - \gamma)\kappa \text{ for } \kappa \to 0_+, \tag{39}$$

cf. 'Appendix B'. Thus, according to (37) and (39), increasing κ (starting from $\kappa = 0$) will lower the critical flow speed. It is noted, finally, that the Coriolis force term and the centrifugal force term, that is, the 'new' terms in the last line of (37), do not depend on the Theodorsen function. Plots showing the true values of κ, $F(\kappa)$ and $\bar{G}(\kappa)$ as function of the flow speed u, corresponding to the eigenvalue curves in Figs. 7, 9 and 11, are given in Appendix C.

---

[3] In Fung [14], the notation $C(\kappa) = F(\kappa) + iG(\kappa)$ is used, but in the present context, the notation (34) is more convenient.

6 Conclusion

The present paper has considered the dynamics of a flapping flag, employing the mathematical model of Argentina and Mahadevan [2], with the aim of clarifying (i) the effect of the complex Theodorsen function on the stability (flutter) bound and (ii) the physical mechanism of the flutter instability.

As to (i), it was shown through an energy balance analysis that a small imaginary part in the Theodorsen function, $C = 1 - \mathrm{i}\,\epsilon$, $0 < \epsilon \ll 1$, has a destabilizing effect, i.e., the critical flow speed u_c is smaller by this approximation than by the quasi-steady approximation $C = 1 - \mathrm{i}\,0$. This prediction gives support to the numerical eigenvalue analyses, which display the same effect, in opposition to earlier studies. It is noted that these studies considered critical flow speed curves (stability diagrams) only, not the distribution of the eigenvalues for lower and higher flow speeds than the critical one. The present study emphasizes the importance of tracing the eigenvalue branches (characteristic curves) for $0 < u < u_c$.

It was found, also, that the last two terms in the expression for the pressure difference across the flag (4), corresponding to a Coriolis force term and a centrifugal force term, respectively, have a significant effect on the stability of the flag and thus, cannot be neglected.

As to (ii), the energy balance analysis showed that a necessary condition for flutter to occur is that the gradient of the phase angle distribution function, $\partial\phi(\xi)/\partial\xi$, is negative over most part of the flag domain, $0 \le \xi \le 1$. This means that the flutter motion is a downstream traveling wave motion, with a 'dragging' appearance (similar, at least in principle, to the motion of a swimming eel [20]).

In the field of optimum design of structures under circulatory loads, it is well known that the critical (flutter) load (or flow speed) may be a non-smooth function of the parameters [19,30] and thus that it is 'dangerous' to just trace the critical load by, say, a root-finding algorithm. Claudon [8] wrote, in the concluding remarks in such a study that, 'In general, it is concluded that characteristic curves as complete as possible should be drawn when analyzing the stability of a structure which becomes unstable by flutter.' The present work confirms and reemphasizes this conclusion.

A Convergence

Table 1 shows the convergence of the critical flow speed u_c and corresponding flutter frequency ω_c in terms of the number of finite elements N_e. The results in columns 1–4 are for the quasi-steady case with $C(\kappa) \equiv 1 - \mathrm{i}\,0$, for the two different mass ratios $\rho = 0.2$ and $\rho = 25$, without inclusion of Coriolis and centrifugal force terms. It is seen that the convergence is more rapid for $\rho = 25$ than for $\rho = 0.2$. Columns 5–8 (marked with asterisks) are for the mass ratios $\rho = 0.2$ and $\rho = 2$, based on the 'full' equation of motion (7), with inclusion of the Coriolis and centrifugal force terms and with proper inclusion of the Theodorsen function $C(\kappa)$. By comparison with the first two columns, it is seen that the convergence speed is not significantly affected by inclusion of the Theodorsen function and the Coriolis and centrifugal force terms.

B Asymptotic values of the Theodorsen function

The asymptotic limits $\kappa \to 0$ and $\kappa \to \infty$ are investigated here for the Theodorsen function

$$C(\kappa) = \frac{H_1^{(2)}(\kappa)}{H_1^{(2)}(\kappa) + \mathrm{i} H_0^{(2)}(\kappa)} \tag{40}$$

with the argument $\kappa = \omega/2u_0$. For $\kappa \ll 1$, it is found that [1]

$$H_0^{(2)}(\kappa) = 1 - \frac{\kappa^2}{2^2} + O\!\left(\kappa^4\right) - \mathrm{i}\left[\frac{2}{\pi}\left\{\ln\left(\frac{\kappa}{2}\right) + \gamma\right\}\left\{1 + \frac{\kappa^2}{2^2} + O\!\left(\kappa^4\right)\right\} + \frac{2}{\pi}\left\{\frac{\kappa^2}{2^2} + O\!\left(\kappa^4\right)\right\}\right], \tag{41}$$

and

$$H_1^{(2)}(\kappa) = \frac{\kappa}{2}\left[1 - \frac{(\kappa/2)^2}{1!\,2!} + O\!\left(\kappa^4\right)\right] + \mathrm{i}\left[\frac{2}{\pi}\frac{1}{\kappa} + \frac{\kappa}{\pi}\left\{1 + \gamma - \ln\left(\frac{\kappa}{2}\right)\right\} + O\!\left(\kappa^3 \ln\kappa\right)\right], \tag{42}$$

Table 1 Convergence of the critical flow speed u_c and corresponding flutter frequency ω_c in terms of the number of finite elements N_e

N_e	u_c $\rho = 0.2$	ω_c $\rho = 0.2$	u_c $\rho = 25$	ω_c $\rho = 25$	u_c $\rho = 0.2^*$	ω_c $\rho = 0.2^*$	u_c $\rho = 2^*$	ω_c $\rho = 2^*$
10	24.19	22.57	3.98	10.46	9.93	15.97	10.52	42.02
20	24.01	22.28	3.95	10.37	9.83	16.06	10.36	42.30
30	23.97	22.22	3.95	10.37	9.80	16.08	10.33	42.45
40	23.96	22.19	3.95	10.37	9.79	16.09	10.32	42.51
50	23.95	22.18	3.95	10.37	9.78	16.10	10.32	42.54
60	23.94	22.17	3.95	10.37	9.78	16.10	10.32	42.56
70	23.94	22.17	3.95	10.37	9.78	16.10	10.32	42.57
80	23.94	22.16	3.95	10.37	9.78	16.10	10.32	42.58
90	23.94	22.16	3.95	10.37	9.78	16.10	10.31	42.59
100	23.94	22.16	3.95	10.37	9.78	16.10	10.31	42.59

Columns 1–4: for the quasi-steady case with $C(\kappa) \equiv 1 - i\,0$, for the two different mass ratios $\rho = 0.2$ and $\rho = 25$. Columns 5–8 (marked with asterisks): for the 'full' equation of motion, with Coriolis and centrifugal force terms, and with proper inclusion of the Theodorsen function $C(\kappa)$, for the mass ratios $\rho = 0.2$ and $\rho = 2$

where γ is Euler's constant, $\gamma = 0.5771\ldots$. These results give that

$$C(\kappa) = 1 - \frac{\pi}{2}\kappa + O(\kappa^2 \ln \kappa) - i\left[\kappa\{\ln 2 - \gamma - \ln \kappa\} + O(\kappa^2 \ln \kappa)\right] \tag{43}$$

for $\kappa \ll 1$. We can go a step further and consider the following series expansion of $\ln \kappa$ [1], valid for $|\kappa - 1| \le 1$:

$$\ln \kappa = (\kappa - 1) - \tfrac{1}{2}(\kappa - 1)^2 + \cdots .$$

Then, (43) can be written as

$$C(\kappa) = 1 - \frac{\pi}{2}\kappa + O(\kappa^2 \ln \kappa) - i\left[\kappa\{\ln 2 + 1 - \gamma - \kappa\} + O(\kappa^3)\right]. \tag{44}$$

For $\kappa \gg 1$, $H_0^{(2)}(\kappa)$ and $H_1^{(2)}(\kappa)$ can be expressed in unified form as [7]

$$H_\nu^{(2)}(\kappa) \sim \left(\frac{2}{\pi\kappa}\right)^{\frac{1}{2}} e^{-i(\kappa - \nu\pi/2 - \pi/4)}\left[1 - i\frac{(\nu^2 - 1/4)}{2\kappa} + O(\kappa^{-2})\right]. \tag{45}$$

This result gives, with $\nu = 0$ and 1, that

$$C(\kappa) \sim \frac{1}{2}\left\{1 + O(\kappa^{-2})\right\} - i\frac{1}{8\kappa}\left\{1 + O(\kappa^{-2})\right\} \tag{46}$$
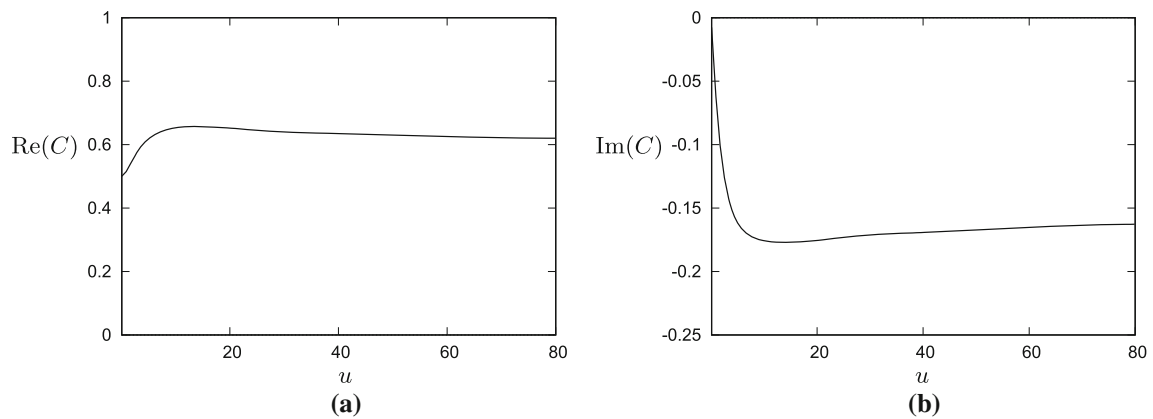
for $\kappa \gg 1$.

C Variation in wake wavenumber and in Theodorsen function with increasing flow speed

Figure 15 shows the wake wavenumber $\kappa = \omega_*/2u$ as function of the flow speed u for $\rho = 0.2$, corresponding to the eigenvalue curves shown in Fig. 7 (without the Coriolis and centrifugal force terms included in (7)). Here, ω_* denotes the imaginary part of the leading eigenvalue, i.e., the eigenvalue with the largest real part. It is noted that $\kappa \to \infty$ for $u \to 0$ and, with reference to Appendix B, that the Theodorsen function $C(\kappa) \sim \frac{1}{2} + i\,0$ for $\kappa \to \infty$. It is seen that κ increases approximately linearly from $\kappa \approx 0.31$ at $u = 10$ to $\kappa \approx 0.42$ at $u = 80$. At the critical flow speed $u_c = 7.05$, $\kappa \approx 0.34$.

Figure 16a, b shows the real and imaginary parts of $C(\kappa)$ as function of the flow speed u for $\rho = 0.2$, evaluated with κ as shown in Fig. 15. Part (a) shows that $Re(C) = F$ decreases approximately linearly from $F \approx 0.66$ at $u = 10$ to $F \approx 0.62$ at $u = 80$. From Part (b), it is seen that $Im(C) = -\bar{G}$ increases, also approximately linearly, from $-\bar{G} \approx -0.18$ at $u = 10$ to $-\bar{G} \approx -0.16$ at $u = 80$. At the critical flow speed $u_c = 7.05$, $F \approx 0.64$ and $-\bar{G} \approx -0.17$.
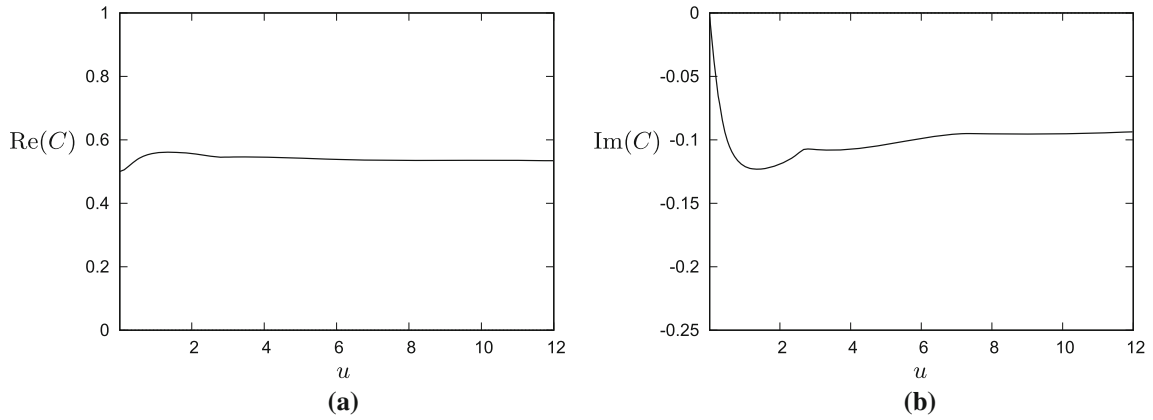
M. A. Langthjem
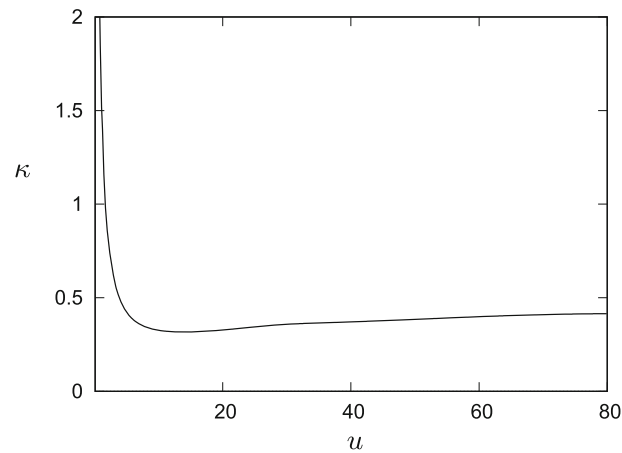
Fig. 15 Wake wavenumber $\kappa = \omega_*/2u$ as function of the flow speed u, for the case $\rho = 0.2$, corresponding to the eigenvalue curves shown in Fig. 7. Here, ω_* is the imaginary part of the leading eigenvalue, i.e., the eigenvalue with the largest real part α_*. It is noted that $\kappa \to \infty$ for $u \to 0$
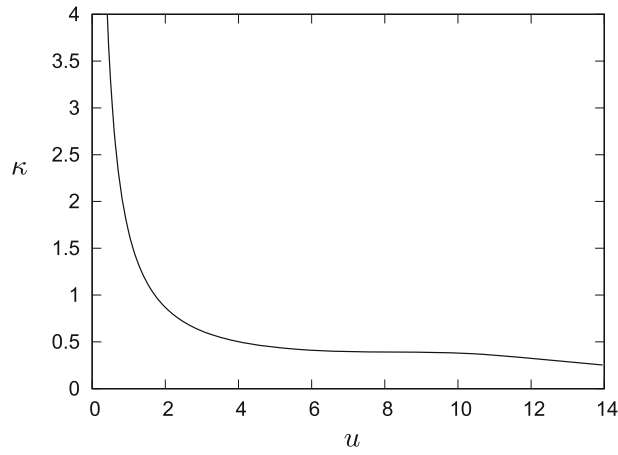

(a)

(b)

Fig. 16 a real and **b** imaginary parts of the Theodorsen function, $F = Re(C(\kappa))$ and $-\bar{G} = \text{Im}(C(\kappa))$, respectively, as function of the flow speed u, when evaluated with the wake wavenumber $\kappa(u)$ shown in Fig. 15 ($\rho = 0.2$)
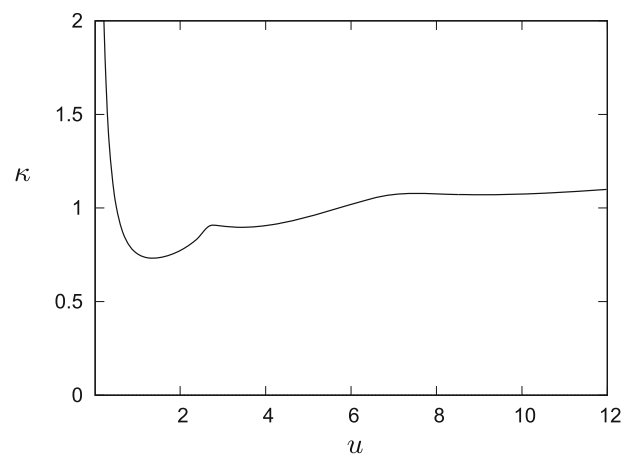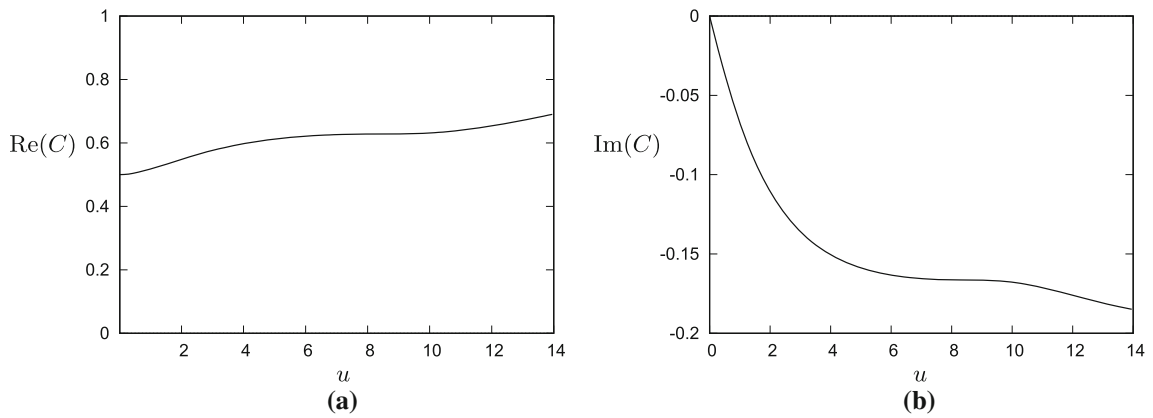

Fig. 17 Wake wavenumber $\kappa = \omega_*/2u$ as function of the flow speed u for the case $\rho = 25$, corresponding to the eigenvalue curves shown in Fig. 9

Fig. 18 a real and **b** imaginary parts of the Theodorsen function $C(\kappa)$ as function of the flow speed u, when evaluated with the wavenumber $\kappa(u)$ shown in Fig. 17 ($\rho = 25$)

Fig. 19 Wake wavenumber $\kappa = \omega_*/2u$ as function of the flow speed u for the case $\rho = 0.2$, corresponding to the eigenvalue curves shown in Fig. 11

Fig. 20 a real and **b** imaginary parts of the Theodorsen function $C(\kappa)$ as function of the flow speed u, when evaluated with the wake wavenumber $\kappa(u)$ shown in Fig. 19 ($\rho = 0.2$)

Figure 17 shows the wake wavenumber $\kappa = \omega_*/2u$ as function of the flow speed u for $\rho = 25$, corresponding to the eigenvalue curves shown in Fig. 9 (again without the Coriolis and centrifugal force terms included in (7)). It is seen that κ increases approximately linearly from $\kappa \approx 0.91$ at $u = 2.8$ to $\kappa \approx 1.1$ at $u = 12$. At the critical flow speed $u_c = 2.82$, $\kappa \approx 0.91$ as well.

Figures 18a, b show the real and imaginary parts of $C(\kappa)$ as function of the flow speed u, for the κ distribution shown in Fig. 17. In the range $u \in [2.8, 12]$, these functions change approximately linearly too: $Re(C) = F$ decreases from 0.55 to 0.53 (Part (a)), while $Im(C) = -\bar{G}$ increases from -0.11 to -0.094 (Part (b)). At the critical flow speed $u_c = 2.82$, $F \approx 0.55$ and $-\bar{G} \approx -0.11$.

Figure 19 shows the wake wavenumber $\kappa = \omega_*/2u$ as function of the flow speed u for $\rho = 0.2$, corresponding to the eigenvalue curves shown in Fig. 11 (in this case with inclusion of the Coriolis and centrifugal force terms in (7)). Here, κ decreases approximately linearly from $\kappa \approx 0.5$ at $u = 4$ to $\kappa \approx 0.25$ at $u = 14$. This behavior, different from the previous two cases, can be understood from Fig. 11b, which shows that the frequency parameters (the imaginary parts of the eigenvalues) here decrease with increasing flow speed. At the critical flow speed $u_c = 9.78$, $\kappa \approx 0.38$.

Figures 20a, b show the real and imaginary parts of $C(\kappa)$ as function of the flow speed u, for the κ distribution shown in Fig. 19. As in the previous cases, in the range where κ varies approximately linearly with u, these functions vary approximately linearly too. In the range $u \in [4, 14]$, $Re(C) = F$ increases from 0.60 to 0.69 (Part (a)), while $Im(C) = -\bar{G}$ decreases from -0.15 to -0.18 (Part (b)). At the critical flow speed $u_c = 9.78$, $F \approx 0.63$ and $-\bar{G} \approx -0.17$.

References

1. Abramowitz, M., Stegun, I.A.: Handbook of Mathematical Functions. Dover Publications, New York (1972)
2. Argentina, M., Mahadevan, L.: Fluid-flow induced flutter of a flag. Proc. Nat. Acad. Sci. **102**, 1829–1834 (2005)
3. Batchelor, G.K.: An Introduction to Fluid Dynamics. Cambridge University Press, Cambridge (1967)
4. Bishop, R.E.D., Johnson, D.C.: The Mechanics of Vibration. Cambridge University Press, Cambridge (1960)
5. Bisplinghoff, R.L., Ashley, H., Halfman, R.L.: Aeroelasticity. Dover Publications, New York (1996)
6. Bolotin, V.V.: Nonconservative Problems of the Theory of Elastic Stability. Pergamon Press, Oxford (1963)
7. Carrier, G.F., Krook, M., Pearson, C.E.: Functions of a Complex Variable: Theory and Technique. SIAM, Philadelphia (2005)
8. Claudon, J.L.: Characteristic curves and optimum design of two structures subjected to circulatory loads. J. de Mèchanique **14**, 531–543 (1975)
9. Coene, R.: Flutter of slender bodies under axial stress. Appl. Sci. Res. **49**, 175–187 (1992)
10. Cook, R.D., Malkus, D.S., Plesha, M.E.: Concepts and Applications of Finite Element Analysis. Wiley, New York (1989)
11. Fahy, F.: Sound and Structural Vibration: Radiation, Transmission and Response. Academic Press, London (1985)
12. Feynman, R.P., Leighton, R.B., Sands, M.: The Feynman Lectures on Physics, vol. 1. Addison-Wesley, Reading, MA (1963)
13. Fitt, A.D., Pope, M.P.: The unsteady motion of two-dimensional flags with bending stiffness. J. Eng. Math. **40**, 227–248 (2001)
14. Fung, Y.C.: An Introduction to the Theory of Aeroelasticity. Dover Publications, New York (1993)
15. Hodges, D.H., Pierce, G.A.: Introduction to Structural Dynamics and Aeroelasticity. Cambridge University Press, Cambridge (2002)
16. Lamb, H.: Hydrodynamics. Cambridge University Press, Cambridge (1993)
17. Lancaster, P.: Lambda-Matrices and Vibrating Systems. Dover Publications, New York (2002)
18. Langthjem, M.A., Sugiyama, Y.: Vibration and stability analysis of cantilevered two-pipe systems conveying different fluids. J. Fluids Struct. **13**, 251–268 (1999)
19. Langthjem, M.A., Sugiyama, Y.: Dynamic stability of columns subjected to follower loads: a survey. J. Sound Vibr. **238**, 809–851 (2000)
20. Lighthill, M.J.: Hydromechanics of aquatic animal propulsion. Annu. Rev. Fluid Mech. **1**, 413–446 (1969)
21. Lighthill, J.: Waves in Fluids. Cambridge University Press, Cambridge (1978)
22. Lighthill, J.: An Informal Introduction to Theoretical Fluid Mechanics. Oxford University Press, Oxford (1986)
23. Manela, A., Howe, M.S.: On the stability and sound of an unforced flag. J. Sound Vibr. **321**, 994–1006 (2009)
24. Manela, A., Howe, M.S.: The forced motion of a flag. J. Fluid Mech. **635**, 439–454 (2009)
25. Milne-Thomson, L.M.: Theoretical Hydrodynamics. Dover Publications, New York (1996)
26. Païdoussis, M.P.: Fluid–Structure Interactions. Slender Structures and Axial Flow, vol. 1, 2. Elsevier, Amsterdam (2013)
27. Païdoussis, M.P.: Fluid–Structure Interactions. Slender Structures and Axial Flow, vol. 1, 2. Elsevier, Amsterdam (2016)
28. Pedersen, P.: Sensitivity analysis for non-selfadjoint systems. In: Komkov, V. (ed.) Sensitivity of Functionals with Applications to Engineering Sciences, pp. 119–130. Springer, Berlin (1984)
29. Rayleigh, Lord: On the instability of jets. Proc. Lond. Math. Soc. **10**, 4–13 (1878)
30. Ringertz, U.T.: On the design of Beck's column. Struct. Optim. **8**, 120–124 (1994)
31. Shelley, M.J., Vandenberghe, N., Zhang, J.: Heavy flags undergo spontaneous oscillations in flowing water. Phys. Rev. Lett. **94**, 094302 (2005)
32. Shelley, M.J., Zhang, J.: Flapping and bending bodies interacting with fluid flows. Annu. Rev. Fluid Mech. **43**, 449–465 (2011)

33. Sugiyama, Y., Langthjem, M.A.: Physical mechanism of the destabilizing effect of damping in continuous non-conservative dissipative systems. Int. J. Non-Linear Mech. **42**, 132–145 (2007)
34. Sugiyama, Y., Langthjem, M.A., Katayama, K.: Dynamic Stability of Columns Under Nonconservative Forces. Theory and Experiment. Springer, Switzerland (2019)
35. Taneda, S.: Waving motions of flags. J. Phys. Soc. Jpn. **24**, 392–401 (1968)
36. Tang, L., Païdoussis, M.P.: On the instability and the post-critical behavior of two-dimensional cantilevered flexible plates in axial flow. J. Sound Vibr. **305**, 97–115 (2007)
37. Tang, L., Païdoussis, M.P.: The influence of the wake on the stability of cantilevered flexible plates in axial flow. J. Sound Vibr. **310**, 512–526 (2008)
38. Theodorsen, T.: General theory of aerodynamic instability and the mechanism of flutter. NACA Report No. 496, pp. 413–433 (1935)
39. Thwaites, B.: The aerodynamic theory of sails. I. Two-dimensional sails. Proc. R. Soc. Lond. A **261**, 402–422 (1961)
40. Watanabe, Y., Suzuki, S., Sugihara, M., Sueoka, Y.: An experimental study of paper flutter. J. Fluids Struct. **16**, 529–542 (2002)
41. Watanabe, Y., Isogai, K., Suzuki, S., Sugihara, M.: A theoretical study of paper flutter. J. Fluids Struct. **16**, 543–560 (2002)
42. Zhang, J., Childress, S., Libchaber, A., Shelley, M.J.: Flexible filaments in a flowing soap film as a model for one-dimensional flags in a two-dimensional wind. Nature **408**, 835–839 (2000)